

Magnetically Enhanced Mechanical Stability and Super-Size Effects in Self-Assembled Superstructures of Nanocubes

Verner Håkonsen, Gurvinder Singh, Peter S. Normile, José A. De Toro, Erik Wahlström, Jianying He, and Zhiliang Zhang*

Artificial materials from the self-assembly of magnetic nanoparticles exhibit extraordinary collective properties; however, to date, the contribution of nanoscale magnetism to the mechanical properties of this class of materials is overlooked. Here, through a combination of Monte Carlo simulations and experimental magnetic measurements, this contribution is shown to be important in self-assembled superstructures of magnetite nanocubes. By simulating the relaxation of interacting macrospins in the superstructure systems, the relationship between nanoscale magnetism, nanoparticle arrangement, superstructure size, and mechanical stability is established. For all considered systems, a significant enhancement in cohesive energy per nanocube (up to 45%), and thus in mechanical stability, is uncovered from the consideration of magnetism. Magnetic measurements fully support the simulations and confirm the strongly interacting character of the nanocube assembly. The studies also reveal a novel super-size effect, whereby mechanically destabilization occurs through a decrease in cohesive energy per nanocube as the overall size (number of particles) of the system decreases. The discovery of this effect opens up new possibilities in size-controlled tuning of superstructure properties, thus contributing to the design of next-generation self-assembled materials with simultaneous enhancement of magnetic and mechanical properties.


synergy between individual building blocks,^[6,7] including enhanced optical,^[8,9] plasmonic,^[10–12] catalytic,^[10,13,14] electronic,^[13,15] magnetic,^[16,17] and mechanical properties.^[18–21] Furthermore, self-assembled materials can serve as a starting point for advanced fabrication of new materials with unique properties.^[22] Self-assembly of magnetic nanoparticles (NPs) is of special interest due to the possibility to exploit magnetism as an additional degree of freedom in the superstructure fabrication. Here, an external applied magnetic field can be used to control the outcome of the self-assembly process.^[23–27] Although magnetic-field-induced self-assembly at the nanoscale is a very complex process because of the interplay between intrinsic (interparticle interactions) and extrinsic (external stimuli) forces, progress has been made recently to better understand the underlying mechanisms behind self-assembly of magnetic superstructures based on NPs of different sizes and shapes.^[28–34] This knowledge has advanced our understanding to fabricate highly ordered superstructure systems of novel

morphologies which would not form in a nonmagnetic system, including horizontal stripes, vertically aligned rods, and helices, based on small magnetic NPs.^[35] Although self-assembly mechanisms involving magnetic NPs are now becoming more illuminated, properties of the postassembled magnetic superstructure systems, especially how magnetism can be linked with mechanical properties, are yet to be investigated.

1. Introduction

Bottom-up self-assembly has become a robust approach for assembling nanoscale building blocks of different sizes, shapes and materials into highly ordered supercrystals, or superstructures.^[1–5] Such ordered self-assembled supercrystalline solids exhibit extraordinary collective properties resulting from the

V. Håkonsen, Prof. J. He, Prof. Z. Zhang
NTNU Nanomechanical Lab
Department of Structural Engineering
Norwegian University of Science and Technology (NTNU)
Trondheim 7491, Norway
E-mail: zhiliang.zhang@ntnu.no

 The ORCID identification number(s) for the author(s) of this article can be found under <https://doi.org/10.1002/adfm.201904825>.

© 2019 The Authors. Published by WILEY-VCH Verlag GmbH & Co. KGaA, Weinheim. This is an open access article under the terms of the Creative Commons Attribution License, which permits use, distribution and reproduction in any medium, provided the original work is properly cited.

DOI: 10.1002/adfm.201904825

Dr. G. Singh
School of Aerospace
Mechanical and Mechatronic Engineering
University of Sydney
Sydney, NSW 2008, Australia

Dr. P. S. Normile, Prof. J. A. De Toro
Instituto Regional de Investigación Científica Aplicada (IRICA)
and Departamento de Física Aplicada
Universidad de Castilla-La Mancha
13071 Ciudad Real, Spain

Prof. E. Wahlström
Center for Quantum Spintronics
Department of Physics
Norwegian University of Science and Technology (NTNU)
Trondheim 7491, Norway

Magnetic NPs possess a set of unique properties due to their small size. In particular, they are often monodomain, as the exchange energy cost to form domain walls is larger than the reduction in magnetostatic energy.^[36] For sufficiently small sizes (e.g., below around 30 nm for spherical iron oxide NPs at room temperature), the magnetocrystalline anisotropy energy barrier becomes small enough to allow for fast thermally driven macrospin fluctuations between equivalent easy directions (Néel relaxation), a regime referred to as superparamagnetism (when observed in timescales longer than that of the fluctuations).^[37,38] The magnetic domain usually fluctuates coherently, and therefore the collection of atomic spins (constituting a magnetic NP) can be effectively replaced by a single macromoment.

Most studies so far have been focused on the magnetic behavior of self-assembled magnetic superstructures, where remarkable collective magnetic properties have been found.^[16,17,26,30,39] In the recent years, it has been demonstrated that self-assembled magnetic supercrystals comprising spherical iron oxide NPs of size larger than 10 nm, show exceptional mechanical properties resulting from thermally induced crosslinking of organic molecular chains (e.g., oleic acid) coating the NPs.^[40,41] However, prior to the introduction of the strong crosslinked covalent bonds, the cohesion of the supercrystal was attributed exclusively to the interchain van der Waals (vdW) interaction between the overlapping organic chains that coated the NPs. Here, there was no mention of the contribution from the vdW and magnetic interactions between the NP cores, which become increasingly significant for particles larger than 10 nm. Rinaldi et al. investigated the link between magnetic and mechanical properties in individual 100 nm composite NPs with a polycrystalline Co–B core, however, an assembly of these particles was never investigated.^[42,43] In particular, the possible influence of interparticle magnetic interactions on the mechanical properties in systems comprising closely spaced superparamagnetic NPs, has not been addressed to date.

In this work, we uncover for the first time, on the basis of cohesive energy, the intimate relationship between nanoscale magnetism and the mechanical stability in highly ordered self-assembled superstructures based on nanocubes (NCs). The cohesive energy is defined as the energy required to break a material up into isolated building blocks. It has been found to be directly related to the mechanical properties in atomic systems,^[44,45] including elastic modulus,^[46,47] hardness,^[45,48] and tensile strength.^[49,50] Thus, cohesive energy is chosen as a reliable measure of mechanical stability in the magnetic superstructures. Our results reveal that the introduction of magnetism yields additional attractive interactions between the nanoscale building blocks, which has a significant stabilizing effect in terms of increased cohesive energy per NC in the studied (2D and 3D) superstructures. Our work thus advances the field of material science by enabling the design of next-generation self-assembled materials with simultaneous enhancement of magnetic and mechanical properties.

Our model system is a nanocomposite self-assembled system comprised of 12 nm magnetite (Fe₃O₄) NCs coated with a monolayer of oleic acid molecular chains. Magnetite, a soft magnetic material, is chosen here because it yields a small energy barrier for spin flipping in a cubic magnetocrystalline energy landscape.^[51] Magnetic NPs of cubic morphology are particularly interesting in the context of superstructures due to

a packing factor reaching up to 1 (as opposed to, e.g., spheres, which can be packed to a maximum factor of 0.74), allowing for a coupling as strong as possible between the nanoscale building blocks within the superstructure. Furthermore, a closer packing of NPs has shown a direct enhancing effect on the mechanical properties of self-assembled systems.^[52]

In this study, the magnetite NCs are self-assembled into ordered superstructures under a vertical applied magnetic field, due to preferential alignment of NC macrospins along the magnetic field direction. After self-assembly, when the external magnetic field is switched off, the vertically aligned macrospins are able to relax to lower the demagnetizing field, and hence the free energy of the system, resulting in an increase in cohesive energy. Owing to the stochastic nature of spin flipping, we employ the Monte Carlo (MC) simulation method to gain insight into the physics behind spin relaxation in magnetite superstructures. We also perform experimental magnetic measurements to gain insight into the magnetic state of the superstructures. Scanning electron microscopy (SEM) images reveal two different packing arrangements (configurations) of magnetite NCs within the self-assembled superstructures, namely with the NC face ((100)-type) and corner ((111)-type) oriented along the z-axis (vertical). Based on MC simulation results, supported by magnetic measurement, we show how the introduction of magnetic interactions between relaxing macrospins significantly increases the cohesive energy of the obtained superstructures, thus providing increased mechanical stability. In addition, we develop a relationship between nanomagnetism, NP configuration, superstructure size and mechanical stability. A remarkable size effect is observed in the self-assembled systems, where smaller superstructures show lower mechanical stability than larger superstructures. Based on the simulation results, we derive a simple mathematical expression describing the cohesive energy of the considered superstructure systems of any size and configuration. This novel “super-size effect” observed in supercrystals made from NPs (often referred to as “artificial atoms”^[53]), analogous to the conventional size effect displayed in the scale of single NPs (i.e., atomic systems),^[54–56] remains evident beyond the nanoscale far up on the sub-micrometer scale. Our results thus advance our fundamental understanding to design multifunctional materials with tunable properties across different length scales.

2. Theory

The self-assembled system is held together by interparticle interactions, a balance of attractive and repulsive interaction potentials dictating interparticle distance and binding strength. Understanding the underlying potentials is imperative in order to establish an interaction model for use in the MC simulations. In what follows, we first introduce the potentials and their implications, and then introduce the MC method.

2.1. Interaction Model

In this model, a distinction must be made between intra- and interparticle potentials, i.e., mutual interactions between two NCs and interactions governing the orientations of spins in the

individual NCs, respectively. The total energy u_{tot} of interaction can be written as

$$u_{\text{tot}} = u_{\text{vdW}} + u_{\text{steric}} + u_{\text{mag}} + u_{\text{MA}} \quad (1)$$

where u_{vdW} , u_{steric} , u_{mag} and u_{MA} are the vdW, steric repulsion, magnetic dipole–dipole, and magnetocrystalline anisotropy potentials, respectively. u_{vdW} , u_{steric} and u_{mag} are interparticle potentials and will contribute directly to the cohesive energy, whereas u_{MA} is an intraparticle potential and will not contribute directly to the cohesive energy, but rather indirectly as this could change the contribution resulting from u_{mag} . The cohesive energy u_{coh} is positive by convention, and defined as

$$u_{\text{coh}} = -(u_{\text{vdW}} + u_{\text{steric}} + u_{\text{mag}}) \quad (2)$$

Fundamentally, all kinds of matter give rise to a vdW attraction (London dispersion interactions), which serves as an imperative contributor to the mechanical stability of the superstructures in question. The vdW potential for two cubic bodies of size a_0 (12 nm), oriented face to face with center-to-center distance r , is given as^[57]

$$u_{\text{vdW}} = -\frac{A(r)a_0^2}{12\pi} \left[\frac{1}{(r+a_0)^2} + \frac{1}{(r-a_0)^2} - \frac{2}{r^2} \right] \quad (3)$$

where $A(r)$ is the retarded Hamaker constant (see the Supporting Information), equal to 21.0×10^{-20} J for magnetite in vacuum.^[58]

The oleic acid surfactant molecules, of chain length L (calculated to be 2.08 nm), are adsorbed onto the magnetite NC

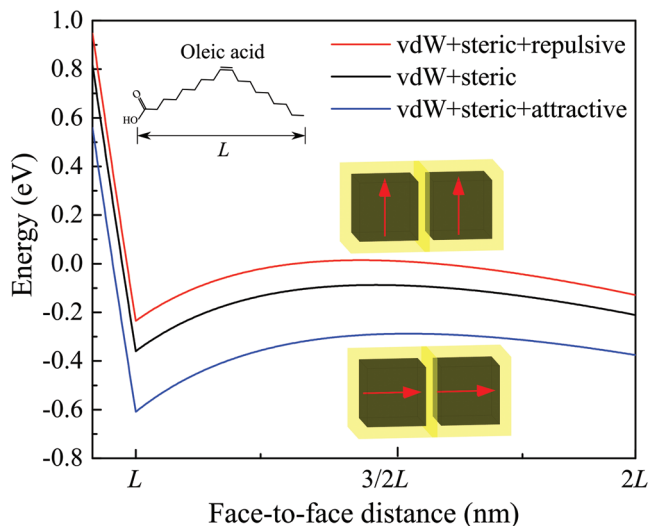


Figure 1. Interaction potentials plotted as a function of face-to-face distance between two approaching 12 nm magnetite NCs coated with oleic acid molecules. The vdW interaction gives rise to an attraction between the NCs, whereas the oleic acid chains give rise to steric repulsion, resulting in an energy minimum at one complete chain length (L) overlap (black curve). Introduction of parallel spins aligned in a side-by-side manner (red curve) and head-to-tail manner (blue curve), results in an additional repulsive and attractive potential, respectively. In all cases, the energy minimum occurs at a face-to-face distance of one oleic acid chain length, L .

surface and give rise to steric repulsion upon chain overlap of two approaching particles (Figure 1). In this model, based on Flory–Huggins theory and Flory network theory,^[59,60] steric interaction potentials in three different regimes are considered as follows

$$u_{\text{steric}} = \begin{cases} 0, & r > a_0 + 2L \\ u_{\text{mix},1}, & a_0 + L < r < a_0 + 2L \\ u_{\text{mix},2} + u_{\text{elastic}}, & a_0 < r < a_0 + L \end{cases} \quad (4)$$

When the NCs are separated with a center-to-center distance of $r > a_0 + 2L$, i.e., longer than two surfactant chain lengths, the steric potential is equal to zero. As the cubes approach each other further, in the regime $a_0 + L < r < a_0 + 2L$, free energy of mixing due to chain volume overlap gives rise to a repulsive potential, as a result of a suppression of configurational degrees of freedom lowering the overall entropy of the system. This potential, $u_{\text{mix},1}$, is given for two cubes of size a_0 in a face-to-face configuration as

$$u_{\text{mix},1} = 2k_B T \frac{a_0^2}{V_s} \phi_{\text{av}}^2 \left(\frac{1}{2} - \chi \right) (a_0 + 2L - r) \quad (5)$$

where k_B is the Boltzmann constant, T is the temperature, V_s is here the average volume of an oleic acid molecule, χ is the Flory parameter, and ϕ_{av} is the volume fraction of the surfactant chains to the volume of the shell in which the surfactants are located (see the Supporting Information). As the cubes are getting closer together, and the overlap starts to exceed one chain length L (i.e., in the region $a_0 < r < a_0 + L$), the free energy of mixing increases further and the potential is calculated according to

$$u_{\text{mix},2} = 2k_B T \frac{a_0^2}{V_s} \phi_{\text{av}}^2 L \left(\frac{1}{2} - \chi \right) \left(\frac{2L}{r - a_0} - 1 \right) \quad (6)$$

In this third regime, elastic compression of the chains as they are compressed between two NC cores, will serve as an additional term in the steric repulsive potential.^[60] The elastic contribution is given as

$$u_{\text{elastic}} = 2\nu k_B T a_0^2 \ln \left(\frac{L}{r - a_0} \right) \quad (7)$$

in which ν is the number of adsorbed oleic acid molecules per unit NC surface area. Any attractive interactions between surfactant chains (i.e., vdW) of two interacting NCs are disregarded in this model. It has been shown that such interchain attractions, resulting from the ordering and interdigitating of overlapping surfactants from two interacting NPs, could be important for the stability of nanocomposite systems comprising small NPs (<6 nm) in vacuum/air.^[18,20,61,62] This holds true if the vdW attraction between cores is screened at a face-to-face distance longer than L (see the Supporting Information), which is generally the case if the particle cores are very small with surfactant chain lengths comparable to or longer than the core size. When the particle cores are large, however, the vdW interaction between cores will cause an attraction leading to an interparticle distance at which the surfactant interchain interactions become purely repulsive after solvent evaporation.^[61,62] In addition, oleic acid monolayers, exhibiting a bend (double bond) in the molecular chain (Figure 1), have been found to yield a low degree of interdigitating in nanocomposites.^[63]

The magnetite NCs are small ferrimagnetic materials, i.e., so small that we can assume only one magnetic domain within each NC.^[37] Magnetic dipole–dipole interactions account for the magnetic potential between two NCs with magnetic moment unit vectors \mathbf{M}_i and \mathbf{M}_j , separated by the distance $|\mathbf{r}_{ij}|$ ^[28,64]

$$u_{\text{mag}}(\mathbf{r}) = \frac{\mu_0 m^2}{4\pi} \left[\frac{\mathbf{M}_i \cdot \mathbf{M}_j}{|\mathbf{r}_{ij}|^3} - 3 \frac{(\mathbf{M}_i \cdot \mathbf{r}_{ij})(\mathbf{M}_j \cdot \mathbf{r}_{ij})}{|\mathbf{r}_{ij}|^5} \right] \quad (8)$$

in which μ_0 is the magnetic permeability in vacuum, and m is the NC magnetic moment estimated to be $80\,550 \mu_B$, where μ_B is the Bohr magneton, by assuming 90% of the magnetite bulk saturation magnetization (see the Supporting Information). The magnetic moment of each NC is considered to be a point dipole positioned in the center of mass of the cube. In this work, the terms magnetic moment and spin are used interchangeably (electron spins give rise to magnetic moments which are aligned antiparallel to each other).

The orientation of the magnetic moment inside each NC is governed by the magnetocrystalline anisotropy, which for magnetite is of cubic symmetry. The potential is given as follows

$$u_{\text{MA}}(\mathbf{M}') = K_A V \left[(M'_x M'_y)^2 + (M'_x M'_z)^2 + (M'_y M'_z)^2 \right] \quad (9)$$

where \mathbf{M}' is the unit vector of the magnetic moment with reference to the cube axes, K_A is the cubic anisotropy constant, which for magnetite is equal to $-1.3 \times 10^4 \text{ J m}^{-3}$, and V is the magnetic volume of the particle in question.^[65,66] This intraparticle potential displays energy minima along the cube diagonals, and thus defines the $\langle 111 \rangle$ -directions as the magnetic easy axes. Since this potential scales directly with the volume of the particle, a magnetic single domain NP below a certain size yields a small enough energy barrier for thermally driven coherent spin flipping between equivalent easy directions, governed by the Néel relaxation mechanism.^[38] This lays the foundation for superparamagnetism. The NCs considered in this study are given the size 12 nm, in addition to being a soft magnetic material with low K_A absolute value, and are thus in the superparamagnetic state at room temperature.^[51]

2.2. Monte Carlo Method

Simulations are carried out by utilizing the classic random-walk Monte Carlo method (Markov chain), with the Metropolis–Hastings algorithm in the canonical ensemble. Superstructure systems of two different NC configurations are created, based on experimental results, in which the NCs are aligned with one of the $\langle 100 \rangle$ - and $\langle 111 \rangle$ -directions along the z -axis (Figure 3b,c), respectively. These alignments give rise to two different kinds of superstructural configurations, exhibiting square and hexagonal cross sections. For the $\langle 100 \rangle$ -configuration, square cross sections of $n \times n$ cubes, with n ranging from 2 and up to 6, are considered. For the $\langle 111 \rangle$ -configuration, the cross section exhibits in-plane hexagonal symmetry, and the number of nearest cube neighbors in a straight line through the center of the cross section is regarded as n , starting from 3 and ranging up to 11 solely through odd numbers (even numbers would

break the hexagonal symmetry). For both the $\langle 100 \rangle$ - and $\langle 111 \rangle$ -types, the number of particles stacked heightwise in layers, h , is ranging from 1 to 16. In the case of the $\langle 100 \rangle$ -configuration, the square cross section is stacked heightwise in layers on top of each other forming a simple cubic lattice, whereas for the $\langle 111 \rangle$ -configuration the layers are stacked heightwise in a face-centered-cubic (fcc) manner (Figure S1, Supporting Information).

The systems of particles are kept translationally static while only the macrospin of each particle is allowed to fluctuate in a stepwise manner in the cubic magnetocrystalline energy landscape. Based on the interaction model between two NCs coated with oleic acid (Figure 1), the interparticle face-to-face distance is chosen to be L , i.e., one complete surfactant chain length overlap, which is situated in the energy minimum. This is also consistent with experimental measurements (i.e., ≈ 2 nm). Any kind of interactions with an underlying substrate are neglected in this study. All simulations are carried out at a temperature of 298 K, and the number of iterations per steps is set to 10^5 , unless stated otherwise. Generally, we observe that most of the relaxation from the aligned initial state (with convergence toward thermal equilibrium) happens during the course of the first 10^4 steps of the simulation, and therefore we choose 10^5 steps to obtain adequate statistics of the system in equilibrium. More information about the MC model is available in the Supporting Information.

3. Results

3.1. Self-Assembly of Magnetic Superstructures

Monodisperse magnetite NCs are synthesized by thermal decomposition of an iron oleate precursor. A high-resolution transmission electron microscopy (TEM) image of a single NC is shown in Figure 2a, together with a schematic of the $\langle 100 \rangle$ - and $\langle 111 \rangle$ -directions of the cube, i.e., the magnetic hard and easy directions, respectively. The NC size distribution (based on 300 counts) is shown in the scanning transmission electron microscopy (STEM) image in Figure 2b, with the measured NC sizes fitted to a lognormal distribution. The mean of the NC size distribution is between 12 and 13 nm, with a standard deviation of 1 nm. Based on this we use a size value of 12 nm for our model system.

Self-assembled magnetic superstructures are fabricated by the evaporation of hexane solution containing dispersed magnetite NCs, at the liquid–air interface under an external magnetic field, as illustrated in Figure 3a. We use an electromagnetic setup with an applied vertical gradient magnetic field (1200 Oe, gradient 300 Oe cm^{-1}), which generates an attractive force downward, to facilitate the directional self-assembly of NCs into vertical columns or rod-like superstructures as the solvent evaporates (more details in the Experimental Section). Surprisingly, careful analysis of the self-assembled superstructures by SEM reveals the occurrence of superstructures in two different configurations ($\langle 100 \rangle$ and $\langle 111 \rangle$) under the same experimental conditions (Figure 3b,c; Figure S2, Supporting Information). The observation of these two different configurations is consistent with observations in the literature of magnetic $\langle 100 \rangle$ - and $\langle 111 \rangle$ -superstructures self-assembled in

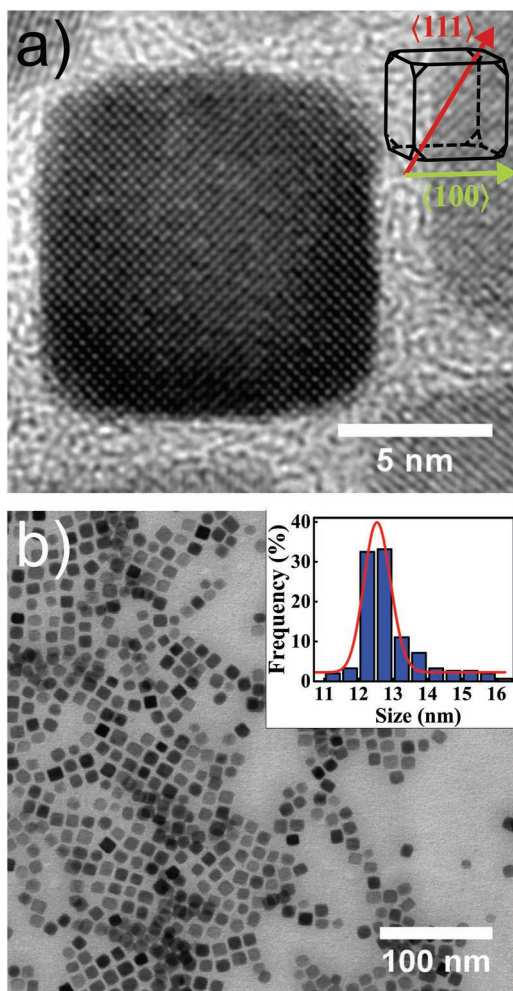


Figure 2. Synthesis of monodisperse magnetite NCs. a) High-resolution TEM image of a single NC, including a schematic of the $\langle 100 \rangle$ - and $\langle 111 \rangle$ -directions of the cube, corresponding to the magnetic hard and easy directions, respectively. b) STEM image showing the size distribution of the synthesized NCs, with the inset showing the measured NC sizes fitted to a lognormal distribution.

horizontal external magnetic fields.^[35] The fact that we observe the $\langle 111 \rangle$ -configuration in the self-assembly experiments, indicates that the NCs in-solution become aligned with the diagonal along the applied magnetic field direction, facilitating growth of $\langle 111 \rangle$ -superstructures, thus confirming the assumption of effective cubic magnetocrystalline anisotropy within the NCs.

The origin of the two different superstructure configurations under identical conditions during self-assembly experiments, is attributed to two different parameters that may vary locally. The first is the local NC concentration, which could vary during solvent drying (which could be uneven), due to significant movement of the solvent as result of magnetic interactions within it (i.e., ferrofluidic behavior). The second parameter is the vertical magnetic field from the electromagnet, which exhibits an in-plane radial variation, i.e., is stronger toward the coils. A stronger vertical magnetic field gradient would favor the $\langle 100 \rangle$ -configuration (Figure 3b) since NCs resting with one of their faces in contact with the substrate would yield a lower magnetic poten-

tial energy than NCs resting on their corner (Figure 3c). In the $\langle 100 \rangle$ -case, the point dipole (located in the cube center of mass) would be situated deeper within the applied gradient field than in the $\langle 111 \rangle$ -case, thus lowering the magnetic potential energy. If the NC concentration in the solvent is locally high during self-assembly, homogeneous superstructure nucleation is more likely to occur at an earlier stage during the solvent evaporation. While the NCs are aligned in the applied magnetic field in the $\langle 111 \rangle$ -configuration in the solvent from before (i.e., locked in one of the easy directions along the applied magnetic field direction), this kind of superstructure configuration is more likely to form in-solution, and is not influenced enough by the gradient of the applied field to render the configuration after formation (Figure S3, Supporting Information). Therefore, for a given applied gradient magnetic field, we propose that there exists a NC concentration threshold above which superstructures exhibiting the $\langle 111 \rangle$ -configuration are favored (as illustrated in Figure S4 in the Supporting Information). Below this concentration threshold, NCs have enough time to be attracted downward by the magnetic field and become pinned down at the diethylene glycol-hexane interface from which heterogeneous nucleation occurs in a $\langle 100 \rangle$ -manner (supplementing SEM images in Figure S5 in the Supporting Information). This NC concentration threshold has already been established for similar systems in a horizontal magnetic field.^[35]

3.2. Simulation of Spin Relaxation in Self-Assembled Superstructures at Room Temperature

Next, we investigate and compare the mechanical stability of self-assembled magnetite superstructures of the two different NC configurations (i.e., $\langle 100 \rangle$ and $\langle 111 \rangle$), by simulating spin relaxation using the MC method. In Figure 3b,c, SEM micrographs show a side view of experimentally obtained superstructures in the $\langle 100 \rangle$ - and $\langle 111 \rangle$ -configurations, respectively, from which the MC models are created. The $\langle 100 \rangle$ -model is given a square cross section (Figure 3b), whereas the $\langle 111 \rangle$ -model is given a hexagonal cross section (Figure 3c). As an example of the $\langle 100 \rangle$ - and $\langle 111 \rangle$ -superstructure, we set in both cases the cross-section parameter $n = 5$, and the height parameter $h = 8$. Both MC-modeled superstructures on the right side of Figure 3b,c are displayed in their initial state prior to spin relaxation, with their spins (red arrows) aligned in the z -direction, which is the direction of the applied magnetic field during self-assembly (dark and yellow cubic boxes are the NC core and oleic acid surfactant layer, respectively).

The spins in the superstructures start to relax immediately as the external magnetic field is switched off, reducing the total interaction energy of the system (Figure 4). Eventually, the total energy (Equation (1)) reaches a plateau, but continues to fluctuate about this plateau as a direct consequence of the thermal energy constantly exciting and relaxing the system (at thermal equilibrium). Figure 4 compares superstructures of different configurations and sizes before and after spin relaxation. Two superstructures of the $\langle 100 \rangle$ -configuration, with $n = \{2, 5\}$, and $h = 5$ in both cases, are shown together with two superstructures of the $\langle 111 \rangle$ -configuration with $n = 3$ (in both cases) and $h = \{2, 8\}$ (Figure 4a). Snapshots of these four superstructures are taken

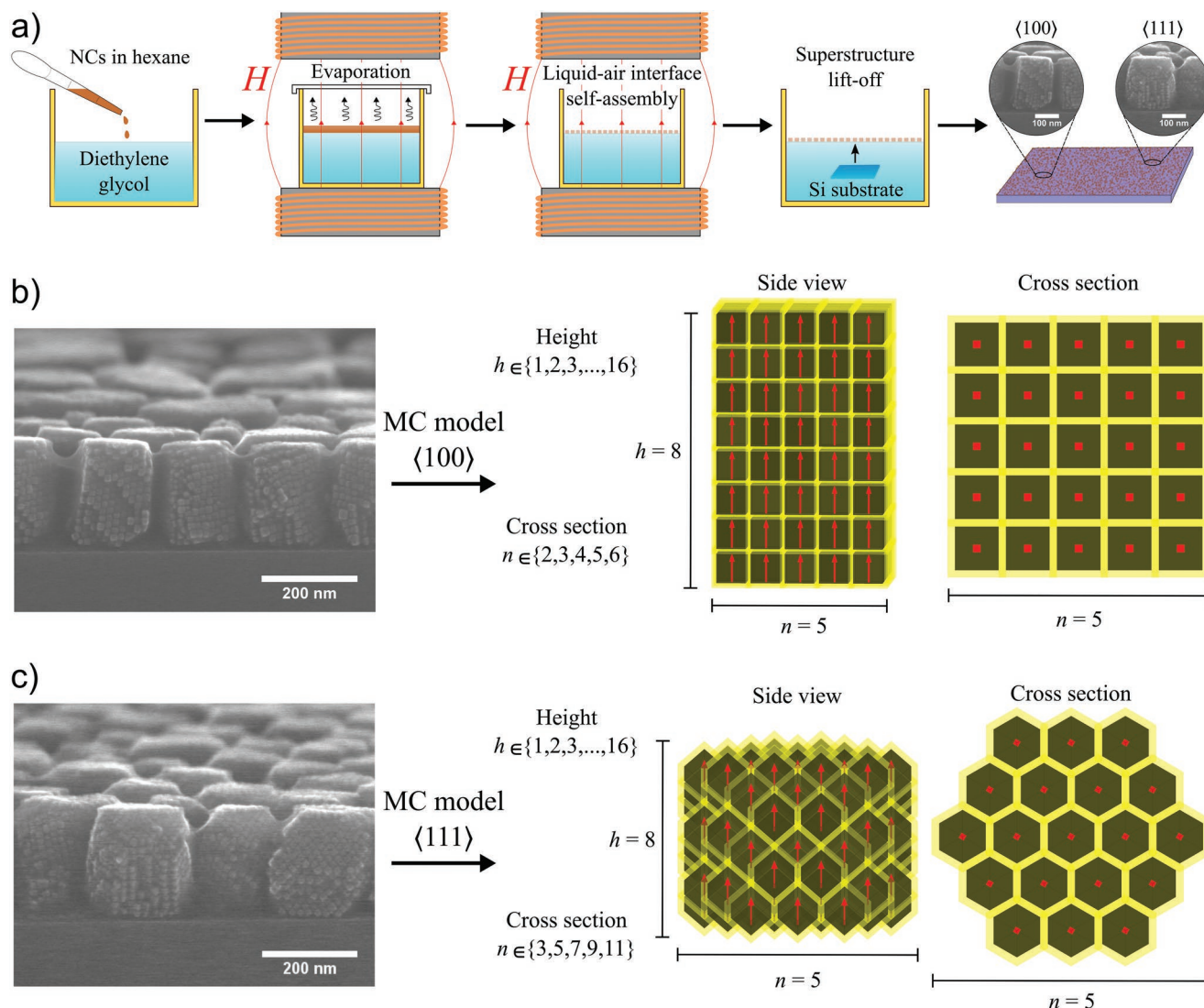


Figure 3. Fabrication of magnetic superstructures and MC modelling. a) Magnetic superstructures are fabricated by self-assembly at the liquid–air interface, onto which magnetite NCs dispersed in hexane are added. A vertical gradient magnetic field (H) is applied, and the solvent evaporates in a closed environment facilitating the in-field self-assembly process. After drying, the self-assembled superstructures (both $\langle 100 \rangle$ - and $\langle 111 \rangle$ -types) are transferred onto a Si substrate through lift-off. Parts (b) and (c) show SEM micrographs of $\langle 100 \rangle$ - and $\langle 111 \rangle$ -type superstructures, respectively, and how the superstructures are modelled in the MC simulations. Here, h and n are the number of cubes stacked in the height and cross section, respectively. In both (b) and (c), a superstructure with $n = 5$ and $h = 8$ is shown, with red arrows indicating the magnetic moment of each NC, here pointing upward in the initial orientation prior to spin relaxation.

after 0 (i.e., initial state) and 10^5 steps in the MC simulation, showing vertically aligned spins in the initial state and apparently randomized orientations in the relaxed state. As an example, different calculated energies (vdW + steric, cohesive and total) as a function of steps in the MC simulation are plotted in Figure 4b after normalization with respect to the number of cubes in the system, for the $\langle 100 \rangle$ -type superstructure with $n = 2$ and $h = 5$. The sum of the vdW and steric energy is constant throughout the simulation since the NC positions are fixed. However, the cohesive energy (plotted here as negative values for comparison) in which the magnetic dipole–dipole energy is included (i.e., sum of interparticle interaction energies), results in an overall variation in the plotted energy. The absolute value of the cohesive

energy immediately starts to increase as the spins relax in the initial steps of the simulation, eventually reaching the mean energy plateau. In the relaxed state, the absolute value of the total cohesive energy is always higher than the vdW- and steric energy contribution. The total energy of the system (per NC) is here the sum of the negative cohesive energy and the intraparticle magnetocrystalline anisotropy energy (Equation (1)), i.e., the energy associated with the orientation of the spin inside the NCs. For magnetite, the magnetocrystalline anisotropy energy at room temperature is always smaller than or equal to zero (more stable close to magnetic easy directions, i.e., the diagonals), thus giving an overall negative contribution to the total energy (a plot of the anisotropy energy contribution to Figure 4b is shown in

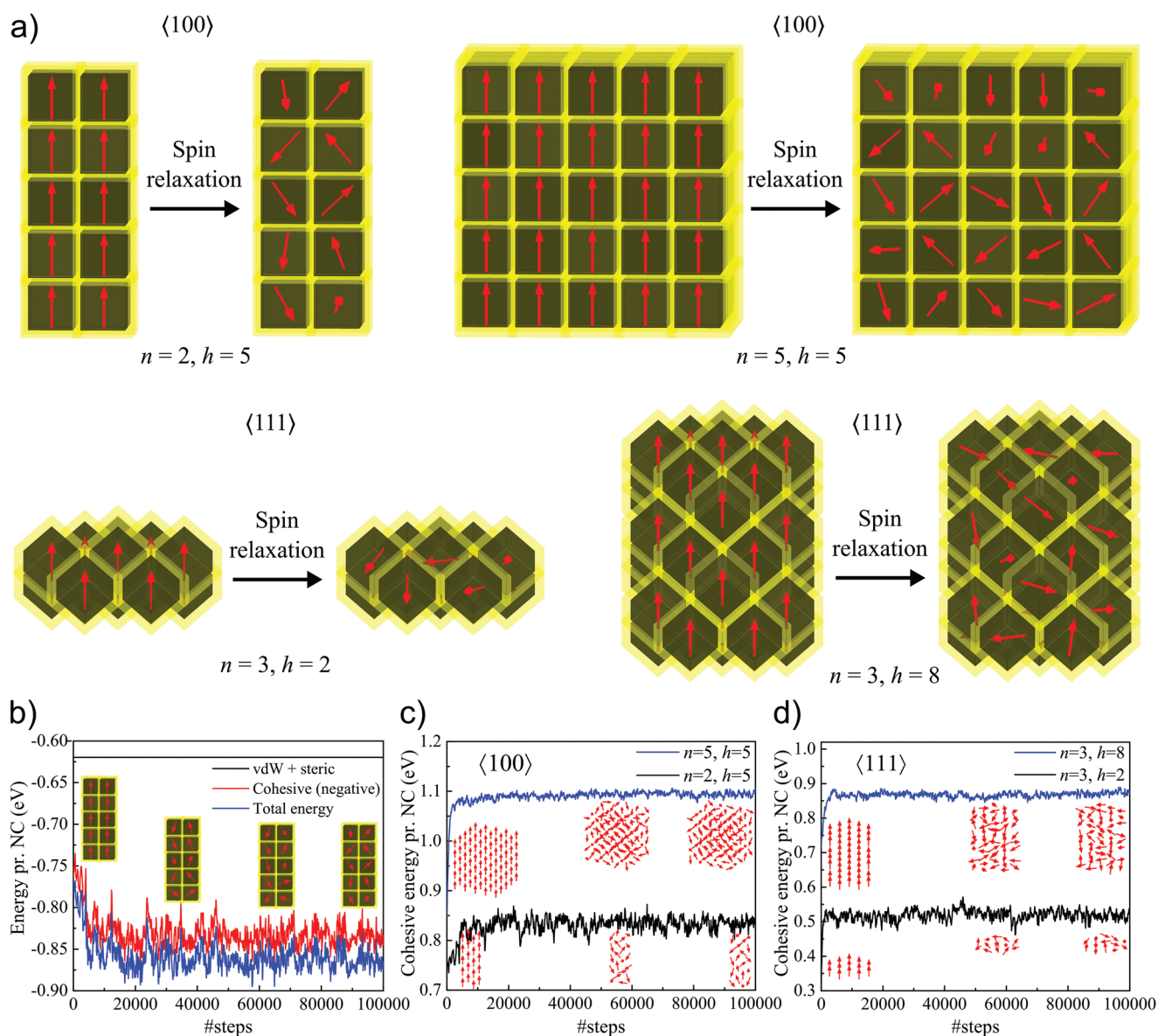


Figure 4. Spin relaxation in superstructures of the $\langle 100 \rangle$ - and $\langle 111 \rangle$ -configurations of different sizes. Immediately after the externally applied magnetic field, keeping the spins vertically aligned, is switched off (at 0 steps in the MC simulation), spin relaxation starts to occur. a) Two superstructures of the $\langle 100 \rangle$ -type with $h = 5$ and $n = \{2, 5\}$, and two of the $\langle 111 \rangle$ -type with $n = 3$ and $h = \{2, 8\}$, are shown before (0 steps) and after spin relaxation (10^5 steps). b) Plotted energies (vdW + steric, cohesive, and total energy) per NC for the $\langle 100 \rangle$ -type superstructure with $n = 2$ and $h = 5$. Snapshots of the superstructure during the simulation are shown. Parts (c) and (d) show the plotted cohesive energy per NC for the superstructures shown in (a), i.e., $\langle 100 \rangle$ - and $\langle 111 \rangle$ -types, respectively. The macrospins of each superstructure are shown in the plot as red arrows during the course of the simulation.

Figure S6 in the Supporting Information). Figure 4c,d illustrate for the $\langle 100 \rangle$ - and $\langle 111 \rangle$ -superstructures, respectively, how the cohesive energy per NC, and thus the mechanical stability, is enhanced as the system size increases. If either the cross section ($\langle 100 \rangle$ -type; Figure 4c) or the height ($\langle 111 \rangle$ -type; Figure 4d) of the superstructure increases, regardless of NC configuration, the cohesive energy per NC increases considerably with a decreasing degree of energy fluctuations, implying a more stable system. Snapshots showing solely the spin orientations are displayed as red arrows in Figure 4c,d.

To compare the mechanical stability between various sizes of magnetic superstructures in the two different configurations

(i.e., $\langle 100 \rangle$ and $\langle 111 \rangle$), we consider the relation between the cohesive energy per NC corresponding to the mean energy plateau, and the aspect ratio of the different superstructures. For both superstructure configurations, the aspect ratio A is defined as the ratio of the number of cubes stacked height-wise, h , to the number of cubes in the cross section, n , i.e., $A = h/n$. The aspect ratio corresponding to the $\langle 100 \rangle$ - and $\langle 111 \rangle$ -configurations is from now on referred to as A_{100} and A_{111} , respectively. Note that due to the different cross-sectional symmetries (i.e., square versus hexagonal) and vertical stacking of NC layers, values of A_{100} and A_{111} corresponding to the same number cannot be compared directly. The results from all MC

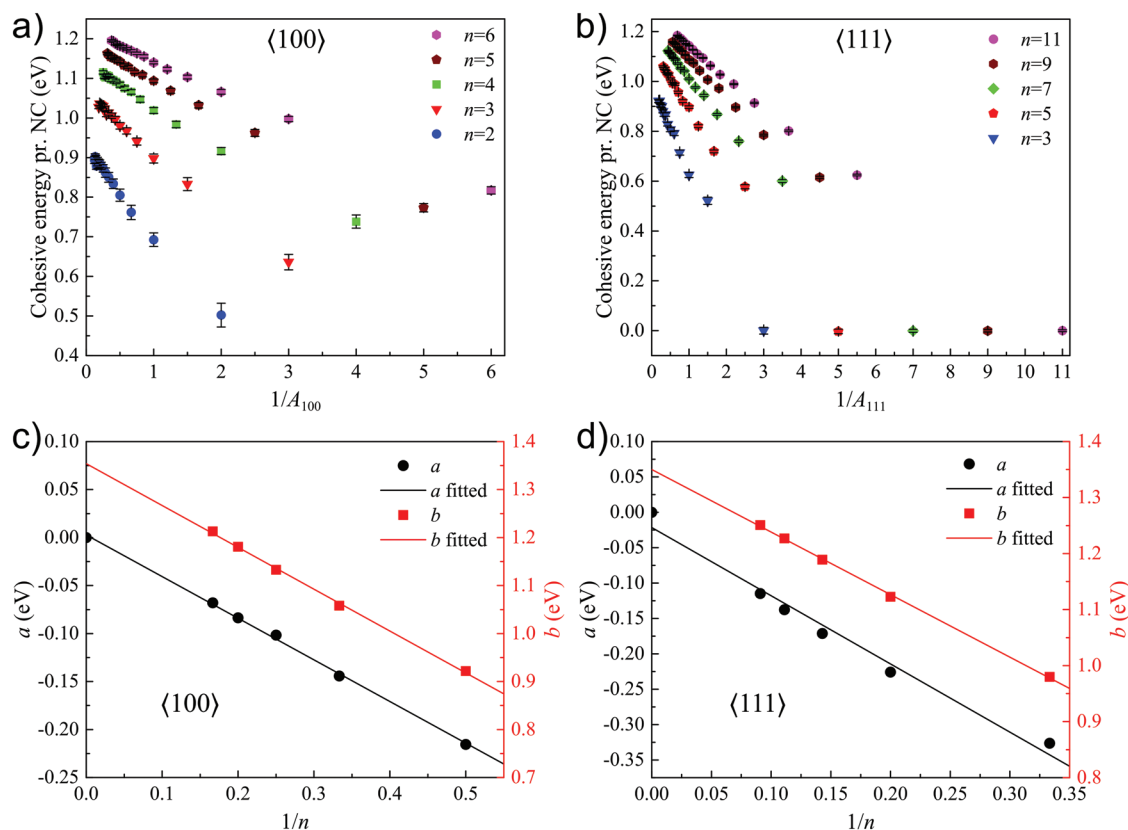


Figure 5. Spin relaxation in superstructures of different aspect ratios and configurations. Parts (a) and (b) show the calculated mean plateau cohesive energies per NC with associated standard deviations, as a function of reciprocal aspect ratio, for the $\langle 100 \rangle$ - and $\langle 111 \rangle$ -configurations, respectively. Linear relationships in the cohesive energy per NC corresponding to superstructures of the same cross section (n -number) are observed in both (a) and (b). In both cases, linear curve fitting has been performed to extract the slopes (a) and y -axis intercepts (b) of the cohesive energies corresponding to superstructures of the same n -number, and the results are shown in (c) and (d). Here, the variables a and b are plotted as a function of reciprocal n -number, displaying a linear relationship.

simulations at room temperature are shown in **Figure 5**, where the cohesive energy per NC for each superstructure is plotted for the $\langle 100 \rangle$ - and $\langle 111 \rangle$ -configurations in Figure 5a,b, respectively. The total energy of the systems is calculated for every 100 steps in the MC simulation of 10^5 steps, and the resulting cohesive energy is considered as it flattens out and reaches a plateau. The cohesive energies per NC for each superstructure of the same configuration are averaged over the plateau (average of 700 data points) and plotted against the reciprocal aspect ratio in the same diagram. Unsurprisingly, larger superstructures, both in n and h , are found to be more mechanically stable than smaller superstructures because on average it requires more energy to remove a NP from a larger structure than from a smaller structure. Interestingly, a linear trend is observed in both cases (Figure 5a,b) with respect to the plotted cohesive energy values corresponding to the same cross section (n -number). Moreover, the absolute value of the slope of this linear relation within the same n -number shows a decreasing trend as the cross section becomes larger, indicating a smaller gain in cohesive energy for higher n -numbers as layers are stacked heightwise on top of each other (i.e., with increasing h).

We further analyze the linearity in the plots of Figure 5a,b to gain deeper insight into the mechanical stability of the self-assembled systems in question. In both cases, linear curve

fitting is performed to extract the slope (a) and y -axis intercept (b) values corresponding to the cohesive energy values of each n -number. The slope and intercept extracted for each n -number for the $\langle 100 \rangle$ - and $\langle 111 \rangle$ -configurations are plotted against the reciprocal of the n -number in Figure 5c,d, respectively. Also here, the results show a linear relationship in both variables a and b as a function of $1/n$. Note in the main plots that due to the obvious decrease in the absolute value of the slope with respect to increasing n (i.e., an increasing negative slope), it is recognized that the slope should approach zero in the limit of infinite cross section n (i.e., when $1/A \rightarrow \infty$), and thus an extra point (0,0) is added to the extracted a -variables in Figure 5c,d for higher accuracy in the following treatment (explanation in Figure S7 in the Supporting Information). Another linear curve fitting is thereafter performed for the variables a and b plotted in Figure 5c,d, to extract parameters from the fitted curves $a = a_1(1/n) + a_2$, and $b = b_1(1/n) + b_2$. The parameters obtained from the curve fitting, including R^2 -values, are reported in **Table 1**. Following the argument above (i.e., $a = 0$ as $n \rightarrow \infty$), the extracted a_2 -values should be as close to zero as possible, which is indeed the case for both the $\langle 100 \rangle$ - and $\langle 111 \rangle$ -types. In any further treatments of the a -variable, the a_2 -parameter is therefore set to zero. With this knowledge, and given the equation $E_{\text{coh}} = a(1/A) + b$ with aspect ratio defined

Table 1. Parameters obtained from linear curve fitting of the a - and b -variables from Figure 5c,d for the $\langle 100 \rangle$ - and $\langle 111 \rangle$ -configurations, respectively, in addition to the ground state (0 K) of the $\langle 100 \rangle$ -configuration (Figure 7b).

NC configuration	$a = a_1(1/n) + a_2$			$b = b_1(1/n) + b_2$		
	a_1 [eV]	a_2 [eV]	R^2	b_1 [eV]	b_2 [eV]	R^2
$\langle 100 \rangle$	-0.434	0.003	0.999	-0.872	1.354	0.999
$\langle 111 \rangle$	-0.964	-0.022	0.981	-1.116	1.350	0.999
$\langle 100 \rangle_{0k}$	-0.429	0.002	0.999	-0.900	1.411	0.999

as $A = h/n$, a closed form expression describing the cohesive energy per NC, E_{coh} , can be derived (details in the Supporting Information)

$$E_{\text{coh}} = \frac{a_1}{h} + \frac{b_1}{n} + b_2 \quad (10)$$

This equation is valid for both the $\langle 100 \rangle$ - and $\langle 111 \rangle$ -type superstructures of any size, as far as the defined cross sections are concerned (i.e., square and hexagonal, respectively). From Equation (10), it is observed that $E_{\text{coh}} = b_2 = E_{\text{bulk}}$ as $h \rightarrow \infty$ and $n \rightarrow \infty$. Therefore, Equation (10) can be rewritten as

$$E_{\text{coh}} = \frac{a_1}{h} + \frac{b_1}{n} + E_{\text{bulk}} \quad (11)$$

The parameters a_1 and b_1 are negative (Table 1), and reflect a decrease in cohesive energy per NC, and hence mechanical stability, when the height and cross section are smaller than the bulk value (i.e., smaller than infinite size). It should be noted that adding another layer for a certain n -number, for instance in the z -direction, in a $\langle 100 \rangle$ -system, is not equivalent to adding another layer in a $\langle 111 \rangle$ -system. This yields different a_1 - and b_1 -values for the two configurations. Hence, the difference in the cross-sectional symmetry, vertical layer stacking, and the number of NCs in the superstructures makes it difficult to directly compare the relative stability of the $\langle 100 \rangle$ - and $\langle 111 \rangle$ -systems on the basis of aspect ratio. However, we can affirm that a monolayer of the $\langle 100 \rangle$ -configuration is more stable than a monolayer of the $\langle 111 \rangle$ -configuration. Monolayers of the $\langle 111 \rangle$ -type have never been observed experimentally, which is explained by the very small calculated cohesive energy per NC (Figure 5b), found to be $\ll k_B T$ at room temperature. Hence, thermal energy alone will destabilize a $\langle 111 \rangle$ -monolayer of any size, resulting in a formation of a $\langle 100 \rangle$ -monolayer instead, which is consistent with findings in the literature.^[67] Furthermore, if similarly sized superstructures of $\langle 100 \rangle$ - and $\langle 111 \rangle$ -systems are compared in terms of the number of NCs, it is clear that the $\langle 100 \rangle$ -system would be more mechanically stable. This is because the average surface NC in the $\langle 111 \rangle$ -type superstructures generally has fewer nearest neighbors than in the surface layer of the $\langle 100 \rangle$ -type, thus reducing the average number of interactions per NC. This difference will, however, eventually cancel out as the two different superstructures start to approach bulk value (i.e., infinite size), where any surface effects disappear.

Owing to the fact that the constituents of the $\langle 100 \rangle$ - and $\langle 111 \rangle$ -systems are the same, as well as the same close packing

of cubes in the interior (not in the surface, as mentioned above) with the same number of nearest neighbors, it is intuitive to expect that the superstructure bulk systems in both cases are equivalent and thus have the same energy. This seems indeed to be the case when comparing the fitting parameter b_2 obtained from the data from both systems (Table 1). The small difference in b_2 -values between systems arises possibly from the effect of the surface layer on spins in the smallest systems considered, which were used as a basis for extrapolation to the bulk value. If we suppress the magnetism from both of the systems, only vdW and steric interaction energies will contribute to the cohesive energy, and the difference in the b_2 values is found to be very close to zero (see Figure S8 and Table S1 in the Supporting Information). These findings also confirm the validity of the interaction models used in the MC simulations.

3.3. Contribution of Spin Relaxation to Cohesive Energy

It is important to understand the contribution of nanomagnetism and spin relaxation to the cohesive energy, and thus mechanical stability, of the systems in question. In order to do so, two different analyses are done to determine the percentage increase (%increase) in cohesive energy caused by spin relaxation. The first analysis encompasses relaxation from the initial vertically aligned state originating from the self-assembly process, and the second the introduction of spins (relaxed) to the nonmagnetic equivalent system (i.e., considering solely vdW and steric energies).

The %increase in cohesive energy resulting from spin relaxation from the initial vertically aligned state is determined for the $\langle 100 \rangle$ - and $\langle 111 \rangle$ -configurations in Figure 6a,b, respectively. Interestingly, the data for the $\langle 100 \rangle$ -superstructures in Figure 6a shows that, apart from the mono- and bilayer case, the %increase in cohesive energy as a function of reciprocal aspect ratio for all system sizes collapses onto the same (master) curve. Hence, superstructures of different sizes exhibiting the same aspect ratio will experience the same %increase in cohesive energy after spin relaxation from the initial state. This result can be understood from a spin positioning standpoint in the prerelaxed structure, where the relative contribution from the repulsion of in-plane neighbors and attraction of out-of-plane neighbors (Figure 1) are the same for aspect ratios of the same value. Monolayers and bilayers deviate from this observation, possibly due to a majority of repulsive contributions to the cohesive energy from the neighboring spins in the prerelaxed state, an effect that is more pronounced for lower n -numbers. This effect will not only cause the mono- and bilayered structures to be less mechanically stable in the prerelaxed state, but also benefit more from spin relaxation in terms of cohesive energy. A %increase in cohesive energy of $\approx 235\%$ (more than three times the initial cohesive energy) is observed for the largest $\langle 100 \rangle$ -monolayer considered in this work, i.e., with $n = 6$. An overall similar trend is observed for the $\langle 111 \rangle$ -configuration (Figure 6b), however the monolayers with different n -numbers show a notably different behavior. In this case, the %increase in cohesive energy appears to be almost constant around 100% for all the $\langle 111 \rangle$ -monolayers. This phenomenon might be purely accidental due the longer center-to-center distance between

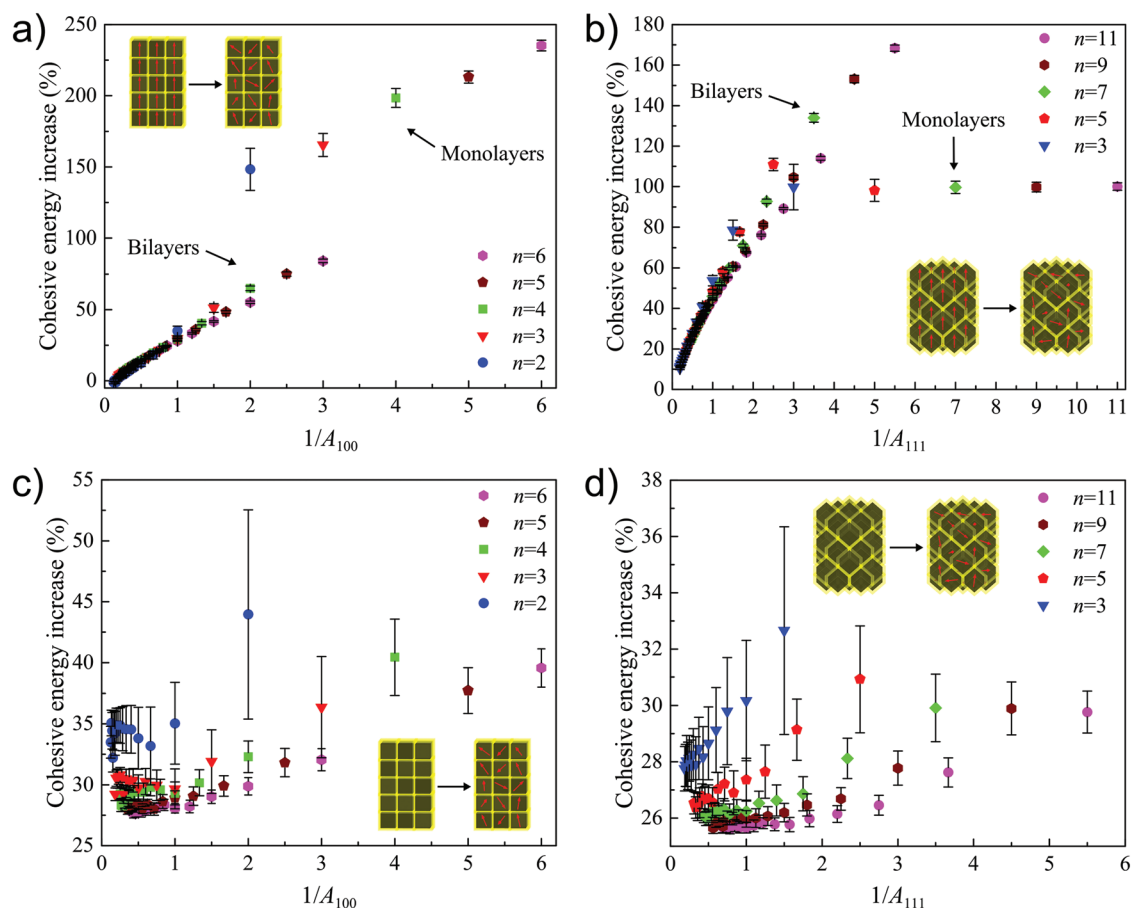


Figure 6. %increase in cohesive energy due to spin relaxation. Parts (a) and (b) show the %increase in cohesive energy as a function of reciprocal aspect ratio, after spin relaxation from the vertically aligned state, for the $\langle 100 \rangle$ - and $\langle 111 \rangle$ -configurations, respectively. As the number of vertical layers (h) exceeds a certain value (2 for $\langle 100 \rangle$, and 3 for $\langle 111 \rangle$), the %increase is the same for structures exhibiting the same aspect ratio. Parts (c) and (d) show the %increase in cohesive energy as a function of reciprocal aspect ratio after the introduction of relaxed spins to the equivalent nonmagnetic systems, for the $\langle 100 \rangle$ - and $\langle 111 \rangle$ -configurations, respectively. The $\langle 111 \rangle$ -monolayers are omitted from (d). Generally, smaller superstructures benefit more than larger ones in terms of mechanical stability from the introduction of magnetism.

cubes in the $\langle 111 \rangle$ -monolayer, relative to the $\langle 100 \rangle$ -case. This causes a perfect balance between vdW forces, steric repulsion and magnetic dipole–dipole interactions in such a way that a larger cross section will not yield any further increase in cohesive energy per NC. This trend disappears for the $\langle 111 \rangle$ -bilayers as interactions between vertical layers become more prominent, resulting in a significant increase in the cohesive energy relative to the monolayers. Triple layers seem to benefit slightly more from spin relaxation than four or more layers, when similar aspect ratio structures are considered. For four layers or more, the %increase in cohesive energy scales with the aspect ratio regardless of size, as shown in Figure 6b. In general, for high aspect ratio structures, the initial state provides for more neighbors in the vertical direction, allowing for maximized head-to-tail interactions which significantly increases the cohesive energy in this state. In this case, spin relaxation from the vertically aligned state could actually have little or no destabilizing effect on the structure, and as a result yield a %change in cohesive energy around zero. No clear effect of shape anisotropy on spin alignment in the relaxed high aspect ratio superstructures is found. Although the cohesive energy per NC

in high aspect ratio superstructures could be slightly lowered relative to the initial aligned state, the mechanical properties will become more isotropic due to randomized spin orientations. This effect is more apparent for the $\langle 100 \rangle$ -structures, whereas for the $\langle 111 \rangle$ -case the spins in two neighboring layers are not vertically aligned, but positioned at an angle of 54.7° relative to each other.

In the second analysis, the %increase in cohesive energy resulting from the introduction of relaxed spins to the nonmagnetic equivalent superstructures (i.e., the sum of the vdW and steric energies) is determined for the $\langle 100 \rangle$ - and $\langle 111 \rangle$ -configurations and shown in Figure 6c,d, respectively. This allows us to determine to what extent nanomagnetism contributes to the cohesive energy of the magnetic superstructures in question. In Figure 6d, $\langle 111 \rangle$ -monolayers appearing around 100% are omitted for easier comparison of higher aspect ratio structures (see complete plot with monolayers in Figure S9 in the Supporting Information). As stated above, a $\langle 111 \rangle$ -monolayer would not be stable enough to form in reality and has thus far never been observed in experiments. From both Figure 6c,d, it is clear that the smallest systems benefit more in terms of mechanical

stability from the introduction of magnetism, although the standard deviation is higher for these structures due to stronger thermal fluctuations. In the case of $\langle 100 \rangle$ -monolayer structures shown in Figure 6c, two different types of NC arrangements within the cross-section are observed depending on the n -number. For $n = \{3, 5\}$, there is only one NC in the center of the structure, while for $n = \{2, 4, 6\}$, there are four NCs in the center. The structures with even n -numbers appear to be more energetically favorable in terms of magnetic dipole–dipole interactions, possibly due to a higher degree of magnetic frustration in cross-sections with odd n -numbers. This effect is not observed in $\langle 111 \rangle$ -superstructures (Figure 6d) because of the presence of one NC in the center regardless of n -number. The %increase in the cohesive energy generally becomes smaller as the systems become larger (both in h and n), for both the $\langle 100 \rangle$ - and $\langle 111 \rangle$ -systems, although some fluctuation in the mean cohesive energy enhancement can be observed in systems with small n -numbers (i.e., especially for $n = \{2, 3\}$). The fact that larger systems benefit less from the introduction of magnetism is possibly a consequence of the different ranges of the vdW and magnetic dipole–dipole interactions. Since the vdW interaction is longer ranged than the magnetic dipole–dipole interaction (i.e., $1/r^2$ compared to $1/r^3$, respectively), larger structures will be stabilized to a higher extent by the vdW interactions, and thus yield a lower %increase from the introduction of magnetism. As the systems become larger and larger, the %increase in cohesive energy from the introduction of magnetism converges toward the bulk value, which is calculated to be 25%.

The two analyses performed above (i.e., relaxation from vertically aligned state and introduction of relaxed spins in an initially nonmagnetic system) combine to provide a complete picture of how magnetism and spin relaxation enhances the mechanical stability of the considered magnetic nanocomposites. The only practical way to fabricate the considered superstructures in this study is by self-assembly in a vertical applied magnetic field, necessarily yielding vertically aligned spins as the initial state. Based on the results summarized in Figure 6, it can be concluded that relaxation from the initial spin state plays a crucial role in the isotropic enhancement of the mechanical stability in magnetic superstructures. In addition, such an equilibration process yields considerably larger cohesive energies compared to the nonmagnetic equivalent systems. Importantly, small superstructures benefit significantly from macrospin relaxation, showing a higher %increase in cohesive energy per NC than larger structures. Yet, in small superstructures the actual cohesive energy per NC is lower than in a larger structure (Figure 5), implying overall less stable systems as the system size decreases.

3.4. Spin Relaxation in Ground State

So far, enhanced superstructure mechanical stability due to spin relaxation has been investigated only at room temperature. However, it is interesting to determine to what extent the magnetic ground state further enhances the mechanical stability (cohesive energy), which will serve as an upper bound in the cohesive energy. To investigate this, we perform simulated cooling from room temperature down to 0 K. Any

temperature-dependencies in all the considered parameters are ignored during cooling, to find the lowest possible energy state at room temperature conditions by eliminating the effect of entropy. For this study, we choose the $\langle 100 \rangle$ -superstructures because they show a relatively simple ground state magnetic pattern for all h and n , and are thus easier to analyze. After reaching the energy plateau (after 10^5 steps at room temperature), the superstructures are subjected to simulated cooling down to 0 K during the course of 3×10^5 steps with a cooling rate of 0.001 K per step. Figure 7a shows the calculated cohesive energy per NC as a function of steps in the MC simulation (the energy is plotted for every 300 steps) during cooling, both with and without the magnetic contribution, for a $\langle 100 \rangle$ -superstructure with $n = 4$ and $h = 12$. The cohesive energy is seen to further increase above the room temperature energy plateau upon cooling until, as expected, reaching a well-defined value at 0 K (after 298 000 steps). Snapshots of the superstructure with associated spin configurations are shown during the course of the simulation, in which the spins become more and more ordered and align along the easy directions, seemingly into series of Landau-like magnetic flux-closure patterns,^[68] below a certain blocking temperature which may be dependent on superstructure size (as well as on the maximum permitted frequency of the fluctuations in the definition of “blocked regime,” which is the MC analogue of the characteristic probing frequency in experimental techniques). However, closer inspection of the system interior reveals a spin ice-like ordering,^[69] with interpenetrating tetrahedral magnetic sublattices (Figure S10, Supporting Information). We stress that a true ground state cannot be guaranteed from these cooling simulations. However, considering the low cooling rate and high degree of spin ordering in the systems at 0 K (high cooling rates yield a higher degree of spin disorder, leading to super-domain formation instead of complete ordering), we believe that any entrapment in metastable states would be close enough to the ground state to not affect the end result. Therefore, we take the obtained cohesive energies at 0 K as the ground state energies. In Figure 7b, the resulting ground state cohesive energies per NC for the $\langle 100 \rangle$ -systems are plotted as a function of reciprocal aspect ratio. Error bars are omitted since the %error was found to be smaller than 0.01% (based on five simulations per superstructure). As in Figure 5a, a linear relationship is also evident for the superstructures of the same cross section n , and the corresponding slopes and y -axis intersects are also found to be linear with respect to $1/n$ (inset of Figure 7b), with the fitted parameters reported in Table 1. Figure 7c,d show the %increase in cohesive energy due to spin relaxation from the vertically aligned state and due to the introduction of magnetism, respectively. The enhancement in cohesive energy from Figure 7c,d is generally found to be higher than the equivalent room temperature calculations shown in Figure 6a,c, respectively, although similar trends are observed. The fluctuations in the mean %increase in smaller structures (especially for $n = \{2, 3\}$) observed in the room temperature case (Figure 6c) are, however, not present in the ground state values of Figure 7d.

Interestingly, the cohesive energy at the ground state is only slightly larger than that obtained at room temperature. For example, in the ground state, the %increase in cohesive energy from the introduction of magnetism (Figure 7d) is calculated

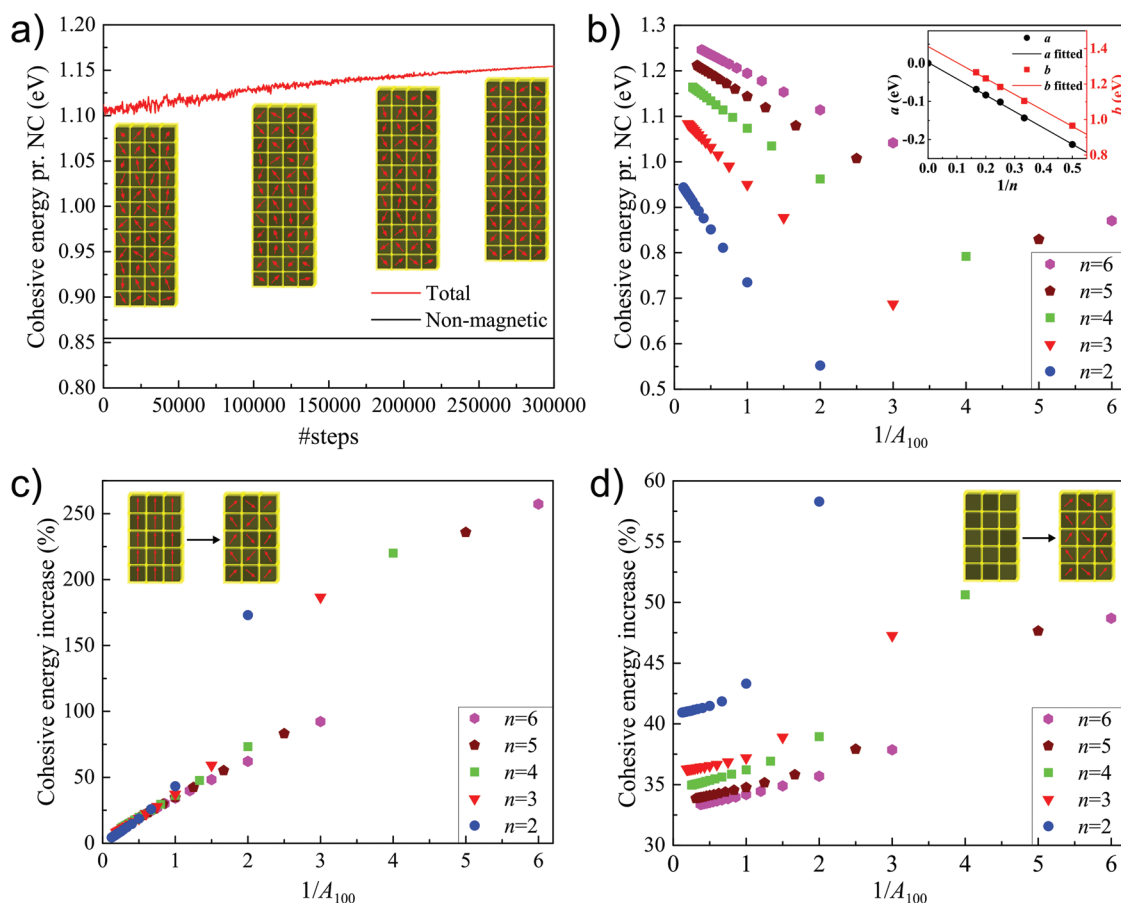


Figure 7. Ground state cohesive energies and their magnetic contribution for the $\langle 100 \rangle$ -configuration. a) Cohesive energies per NC, both total (red curve) and nonmagnetic (black curve), are plotted as a function of the number of steps in the MC simulation for a superstructure with $n = 4$ and $h = 12$. The cooling rate was set to 0.001 K per step, and snapshots are shown during the course of the simulation. b) Results showing the calculated ground state cohesive energies per NC as a function of reciprocal aspect ratio. Results from linear curve fitting of the cohesive energies per NC corresponding to the same n -number are shown in the inset. Parts (c) and (d) show the %increase in cohesive energy as a function of reciprocal aspect ratio due to spin relaxation from the vertically aligned state and due to the introduction of relaxed spins to the equivalent nonmagnetic system, respectively. Similar trends as for the room temperature case are observed, although the values are consistently higher, with no fluctuations. Standard deviations in (b)–(d) have been omitted due to small values.

for the bulk system to be 30%, only 5% higher than the room temperature case. This indicates that the room temperature (mean) spin configuration of randomized spins is not far away from the ordered ground state (dictated by the magnetocrystalline anisotropy) in terms of increased cohesive energy (if we were to consider the magnetocrystalline anisotropy energy contribution to the total energy, this would be considerably lower). In fact, if we investigate the orientation of the macrospins with respect to the magnetic easy directions, we find that the average deviation at room temperature is between the easy and the hard directions, at an angle of $\approx 24^\circ$ (Figure S11a, Supporting Information), whereas at 0 K it is around 10° , indicating that alignment along the easy directions (i.e., at 0° angle) is not the lowest energy configuration (Figure S11b, Supporting Information). Hence, some relaxation happens to balance the magnetic dipole–dipole coupling of neighboring spins and the magnetocrystalline anisotropy from each individual NC. This is particularly clear for the $\langle 100 \rangle$ -monolayers, especially with $n = 6$ ($h = 1$), in which the angular deviation from the easy axes is close to 35° (Figure S12, Supporting Information).

For the $\langle 111 \rangle$ -configuration in the ground state, the magnetic pattern is not as clearly defined as for the $\langle 100 \rangle$ -case, due to the surface effect on spins. This causes spin frustration and random alignment in the surface layer, but in the interior of the superstructure, however, the spins remain ordered at 0 K. This is shown in Figure 8 (both in top and side views) for the largest $\langle 111 \rangle$ -superstructure considered in this study with $n = 11$ and $h = 16$ (simulated by using the same parameters as for the $\langle 100 \rangle$ -case), in which a spin core–shell structure is revealed. Here, the shell consists of disordered spins and the core organizes into a spin ice-like pattern. As the system size approaches bulk size, the properties of the $\langle 111 \rangle$ -structures in the ground state should converge to the bulk $\langle 100 \rangle$ -properties in the ground state.

3.5. Magnetic Measurements of Self-Assembled Superstructures

In order to gain insight into the magnetic state (i.e., magnetic regime, NC magnetic moment and dipolar interaction strength) of the model system in question, the self-assembled

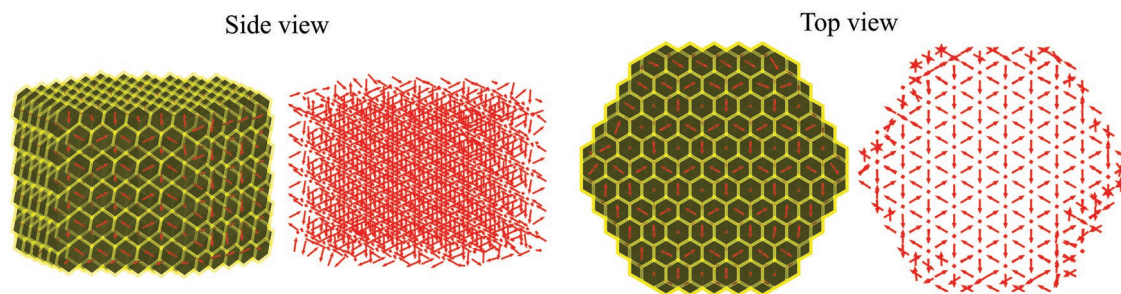


Figure 8. A $\langle 111 \rangle$ -superstructure with $n = 11$ and $h = 16$ is shown in the ground state after simulated cooling from room temperature to 0 K. Both top and side views are shown, with and without the actual NCs present. A spin core–shell structure is seen, in which the shell consists of disordered spins and the core exhibits an ordered spin ice-like pattern.

superstructures are characterized magnetically. Low field ($H = 20$ Oe) zero-field-cooled (ZFC) and field-cooled (FC) magnetization curves are measured both for the ordered assembly of NCs and for a dilute dispersion of NCs in cyclohexane (concentration $17.5 \mu\text{g mL}^{-1}$, measured by inductively coupled plasma mass spectrometry (ICP-MS)), as shown in Figure 9. Both the dilute dispersion (Figure 9a) and the ordered assembly (Figure 9b) show superparamagnetic behavior at room temperature, therefore justifying the assumption of relaxing macrospins in the simulation. The blocking temperature, taken as the ZFC peak temperature, of the ordered assembly is found to be ≈ 200 K, which is ≈ 50 K higher than the blocking temperature of the dilute dispersion at ≈ 150 K. This indicates the presence of strong magnetic dipolar interactions in the assembly, relative to isolated NCs.^[70,71] Furthermore, the observation of a flat-shaped FC curve of the assembly at temperatures below the ZFC peak is also consistent with a scenario of strongly dipole–dipole interacting particles.^[72]

The inset in Figure 9a shows the magnetic response of the NC dispersion at $T = 260$ K, below the freezing point of cyclohexane. From the saturation moment, given the concentration of the dispersion ($17.5 \mu\text{g mL}^{-1}$), we obtain a saturation magnetization of 86 emu g^{-1} , which amounts to 92% of the bulk value, thus validating the NC magnetic moment employed in the simulations ($80\,550 \mu_B$, see the Supporting Information). The fit of the magnetic response, M , to the Langevin function ($M = M_s[\coth(x) - 1/x]$, where $x = m\mu_0 H/k_B T$), and M_s is the NC saturation magnetization) yields a macrospin of only $\approx 54\,400 \mu_B$. This value is, as expected, smaller than that obtained from the saturation moment of the NC dispersion, since the Langevin function neglects the anisotropy energy barrier of the particles (magnetic response measurement at a temperature of at least four times the blocking temperature is, in general, required for Langevin fitting to provide an accurate macrospin value).^[73]

4. Discussion

Based on our results, it is clear that the consideration of nanomagnetism in the nanocomposite magnetite-oleic acid superstructure systems provides a significant mechanically stabilizing effect. A considerable enhancement of the cohesive energy was found for every studied superstructure after including magnetic interactions between NCs, leading to a %increase greater than or equal to 25% (i.e., smallest for bulk systems) at room

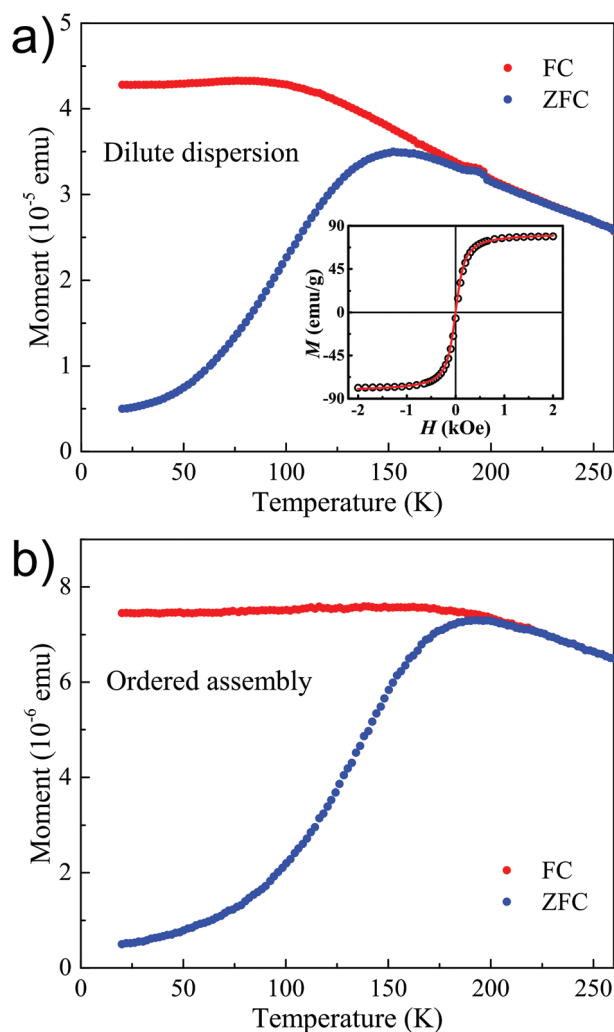


Figure 9. ZFC and FC magnetization curves measured in an applied field of 20 Oe. a) A dilute dispersion of NCs in cyclohexane, measured below the fusion point of cyclohexane. The inset shows the magnetic response of the dispersion at 260 K fitted (red curve) to a simple Langevin function. b) The ordered NC assembly, measured from room temperature. In both cases, the system remains superparamagnetic at room temperature, where the blocking temperature of the ordered assembly is observed to be ≈ 50 K higher than the blocking temperature of the dilute dispersion. Furthermore, the flat shape of the FC curve in (b) at temperatures below the ZFC peak confirms a system of strongly interacting NCs.

temperature, depending on the size of the system. Experimentally, the strong dipolar interactions were evident from the higher blocking temperature in the superstructures compared to that of a dilute system comprising the same NCs (Figure 9b), as well as in the flat aspect of the FC curve of the assembly at low temperature. The driving force behind the actual macrospin relaxation after self-assembly is the reduction in the demagnetizing field, and thus a reduction in its associated energy cost, similar to the driving force behind domain wall formation in ferromagnetic bulk materials. In contrast to bulk materials, the spin fluctuation at room temperature in the magnetic superstructure systems was revealed by the MC simulations to be highly dynamic, driven by the thermal energy. Therefore, the superstructure system as a whole remains superparamagnetic after spin relaxation, in agreement with the experimental results (Figure 9b). Hence, the entropic contribution also plays an important role in the spin relaxation/fluctuation in magnetite superstructures, and thus the degree of fluctuation about the mean energy plateau is expected to increase with increasing temperature (and also with decreasing system size), until the system eventually destabilizes. In the ground state, however, there are no thermal fluctuations.

Qualitatively, the ground state configuration may be understood as resulting from an optimum compromise between i) the alignment along the magnetocrystalline easy axes (the four cube diagonals yielding eight states with the same lowest anisotropy energy), ii) the avoidance of costly (in terms of dipolar energy) heads-on or tails-on spin alignments along the nearest-neighbor directions (vertical and horizontal), and iii) flux-closure alignment to reduce the demagnetizing field, leading to alternate up/down zig-zag directions between columns/rows of NCs. This difference between room temperature and ground magnetic state is illustrated in Figure 10, in which the demagnetizing field is reduced by ordered and disordered spins, respectively. Notably, only a small difference in cohesive energy per NC was found between the room temperature state (considering mean values) and the ground state, although the reduction in fluctuations of small systems close to the ground state will enhance the stability to a greater extent.

The novelty in our findings lies in the nanoscale size of the building blocks constituting the magnetic superstructures. The NP size needs to be small enough to allow for a small enough energy barrier for spin flipping (i.e., superparamagnetism), which can facilitate spin relaxation in a superstructure. At the same time, the NPs need to be large enough to give a significant interior magnetic volume (compared to the disordered surface layer within the NP) resulting in a magnetic moment strong enough to couple with neighboring moments in the superstructure. We have shown that if these criteria are fulfilled, as it is the case for 12 nm magnetite NCs studied here, spin relaxation can enhance the mechanical stability of a magnetic superstructure by providing additional attractive interactions between building blocks. Interestingly, the size of the actual superstructures in both the $\langle 100 \rangle$ - and $\langle 111 \rangle$ -configurations was shown above to have a direct effect on the cohesive energy per NC, and thus the mechanical stability, in these structures. This size effect, which we refer to as a “super-size effect”, indicates a mechanical destabilization of a superstructure through a decrease in cohesive energy per NC, as the systems become smaller with respect to

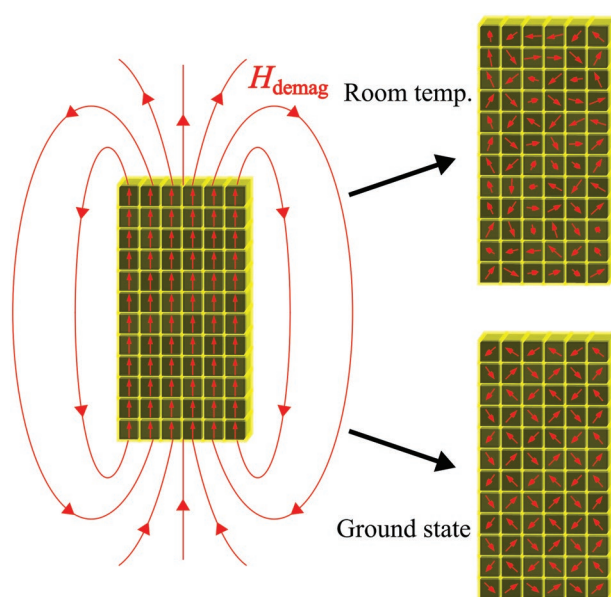


Figure 10. Driving forces behind spin relaxation. The demagnetizing field (H_{demag}) is reduced upon spin relaxation in both the room temperature state and the ground state. In the room temperature state, spin fluctuations will also happen as a result of the thermally driven entropic contribution to the free energy, causing randomized spin orientations. In the ground state, the spins orient themselves into an ordered pattern to cancel out most of the demagnetizing field, avoiding costly (in terms of dipolar energy) heads-on/tails-on spin pairs between nearest neighbors (horizontal and vertical directions), at the same time as the magnetocrystalline anisotropy energy is kept at a minimum. This results in Landau/spin ice-like patterns with alignment close to the magnetic easy axes. In both cases, the mechanical stability is enhanced (i.e., cohesive energy increased), and the mechanical properties become more isotropic.

the number of NCs (first observed in Figure 5, and later derived and described by Equation (11)). Hence, as the size of both the $\langle 100 \rangle$ - and $\langle 111 \rangle$ -superstructures decreases, the mechanical stability decreases. This effect is analogous to the well-known NP size effect, in which the NPs tend to become more and more unstable as their size decreases. The super-size effect, however, is evident also far up on the sub-micrometer scale. Furthermore, NPs are often referred to as “artificial atoms,”^[53] a term that indicates size effects similar to real atomic systems. We confirm this for the first time, justifying the notion of NPs as artificial atoms. To clearly illustrate how the cohesive energy per NC changes with superstructure size, Equation (11) is plotted for the $\langle 100 \rangle$ -configuration in Figure S13a in the Supporting Information, by setting $h = n$ (i.e., a perfect supercube). This curve shows a striking similarity to the cohesive energy per atom in single metallic NPs (Figure S13b, Supporting Information),^[56] but of course at the larger length scale. Furthermore, this discovery adds new opportunities in tuning mechanical properties of superstructured materials, which has not been addressed to date, i.e., through the overall size of the superstructure. Our findings also suggest that there could exist (super-)size effects in other collective properties of self-assembled superstructures, which is a very interesting aspect that should be addressed.

The methodology developed in this work provides a valuable toolkit for calculating cohesive energies, giving insight into the mechanical stability of self-assembled superstructures of

any size provided the cohesive energies for small systems are known. The cohesive energy for systems of any size can be estimated by performing a series of linear curve fitting of only a handful of sizes, as shown in Figure 5, dramatically reducing the demand for computational resources. As a minimum, our method only requires four system sizes, in which two of them have the same cross section or the same height, in order to obtain a crude estimate of the cohesive energy for any superstructure size, including the bulk system. Furthermore, the validity of our method was confirmed for magnetite NPs packed in both a simple cubic and an fcc arrangement. As an additional consistency test, the method remained valid for the equivalent nonmagnetic systems in which only vdW and steric interaction energy contributions were considered (Figure S8 and Table S1, Supporting Information), indicating that the method could also be used for nonmagnetic systems (verification would require the study of self-assembled superstructures made from nonmagnetic NPs, which is beyond the scope of the present study).

Magnetite was used as the material of choice in this study, due to its soft magnetic properties and the dynamic behavior of the spins of individual superparamagnetic NCs, which was found to provide an isotropic mechanical stabilizing contribution to the overall self-assembled superstructure. The cohesive energies calculated in this work correspond to an interparticle separation of a single oleic acid chain length. However, if the NCs are brought closer together, e.g. by the introduction of a shorter surfactant chain length, the mechanical stability is expected to further increase, as well as the contribution of nanomagnetism to the cohesive energy (due to the shorter range and stronger coupling of the magnetic dipole–dipole interaction, compared to the longer ranged vdW interaction). Furthermore, an interesting prospect for future studies is to examine how the mechanical stability relates to similar magnetic superstructures with different magnetocrystalline anisotropy. For instance, cobalt ferrite (CoFe_2O_4), in which one of the Fe atoms per formula unit has been substituted with a Co atom, exhibits easy axes along the $\langle 100 \rangle$ -directions (positive anisotropy constant, K_A) and significantly stronger anisotropy.^[74,75] Understanding the effect of magnetic anisotropy on mechanical properties would be a further significant contribution to the field of self-assembled magnetic superstructures. NC systems should be made translationally dynamic in such simulations, so as translational energy relaxation/fluctuation may contribute to providing a more realistic physical picture of the systems in question.

5. Conclusion

In summary, we presented a MC simulation approach to investigate spin relaxation in experimentally obtained self-assembled nanocomposite magnetite-oleic acid superstructures, made from 12 nm NCs. The MC method has been proven to be a valuable tool to provide in-depth understanding of the magnetic state of the self-assembled magnetic systems. The driving force behind spin relaxation from the vertically aligned state is the reduction in demagnetizing field of the magnetic superstructures, leading to overall additional attractive interactions between NC cores in the superstructures, thus enhancing the mechanical stability signifi-

cantly. Experimental magnetic measurements indicated a system of strongly interacting magnetic particles, which remained superparamagnetic at room temperature, in excellent agreement with the MC simulations. Furthermore, we established the relationship between nanoscale magnetism, NP arrangement (considering $\langle 100 \rangle$ - and $\langle 111 \rangle$ -configurations), superstructure size and mechanical stability in the considered model system. For systems of similar size (in terms of the number of NCs), the $\langle 100 \rangle$ -configuration was found to be more stable than the $\langle 111 \rangle$ -configuration because of the fewer nearest neighbors in the $\langle 111 \rangle$ -surface layer. The effect of superstructure size was thoroughly studied in this work, and the results revealed a lower cohesive energy per NC and higher degree of thermal fluctuations as the size of the superstructure decreases. This causes a mechanical destabilization of smaller sized superstructures, compared to the corresponding bulk superstructure system, analogous to the well-known “size effect” in nanoscience. Based on these findings, we introduced the new term “super-size effect,” indicating a size effect present in superstructure systems that extends beyond the nanoscale, up on the near micrometer scale. This novel super-size effect further justifies the notion of artificial atoms, a term often used for NPs. Based on a handful of MC simulations, we established a closed form mathematical expression describing the cohesive energy per NC for magnetite-oleic acid superstructure systems of any size and configuration (i.e., the considered $\langle 100 \rangle$ - and $\langle 111 \rangle$ -configurations). Our calculation approach was found to be applicable to the same systems after removing the NC magnetic moments, suggesting that it could be used to analyze different (nonmagnetic) superstructure systems.

The calculated %increase in cohesive energy resulting from spin relaxation from the initial vertically aligned spin state was generally found to be dependent on aspect ratio of the superstructures, and not on the actual system size. A significant magnetic contribution to the cohesive energy, and hence the mechanical stability, was found for every relaxed superstructure considered in this study. The introduction of relaxed spins to the equivalent nonmagnetic system at room temperature was shown to increase the cohesive energy of the bulk system by 25%, and beyond this value for smaller systems. Conclusively, smaller systems, although being less stable than larger systems, was shown to benefit more than larger systems from spin relaxation in terms of %increase in cohesive energy, a result which is understood from the shorter interaction range of the magnetic dipole–dipole potential compared to the vdW potential (which is more dominating for larger systems). The magnetic superstructure ground state was established to yield Landau-like patterns of spins oriented close to the magnetic easy axes, but was found to only lead to a slight increase in cohesive energy relative to the room temperature case.

Our findings shed new light on the magnetic state of self-assembled magnetic NP systems, setting up new design criteria for fabricating next-generation superstructured materials with simultaneous enhancement of both magnetic and mechanical properties. The discovered super-size effect in superstructures opens up new possibilities in material science in terms of tuning properties through system size, which is of practical relevance in many areas of research, including energy storage and conversion, biomedical applications, sensing devices, and information technology.

6. Experimental Section

Synthesis of Monodisperse Fe₃O₄ Nanocubes: Fe₃O₄ NCs were prepared by thermal decomposition of iron oleate, according to a protocol previously reported in the literature.^[35] First, iron oleate was prepared by mixing of iron(III) chloride (FeCl₃·6H₂O, Alfa Aesar, 98%) (5.39 g; 20 mmol) and sodium oleate (TCI, >97%) (18.25 g; 60 mmol) in a 250 mL round-bottom flask containing deionized water (30 mL), hexane (70 mL) and ethanol (40 mL). The reaction mixture was vigorously stirred under nitrogen atmosphere for 4 h at $T = 70$ °C. The dark red organic product was separated from the water phase and washed three times with water to remove reaction byproducts. The product was dried in vacuum at room temperature to remove residual water content, hexane and ethanol, and thereafter transferred to a glass vial. The iron oleate product was stored in a fridge ($T \approx 4$ °C). To synthesize Fe₃O₄ NCs, prepared iron oleate (1.62 g) and sodium oleate (0.42 g) were added to a 100 mL round-bottom flask containing octadecene (Sigma-Aldrich, 25 mL). The reaction mixture was heated to 320 °C at the rate of 3 °C min⁻¹ under argon atmosphere, and left at this temperature for 45 min before cooled down to 100 °C. The NCs were obtained after washing the reaction product three times with toluene and isopropanol, and thereafter stored in toluene at room temperature. The size of the Fe₃O₄ NCs was measured to be 12 ± 1 nm (Figure 2).

Magnetic Field-Induced Self-Assembly of Fe₃O₄ Nanocubes: Ordered rod-like superstructures were prepared by means of the liquid–air interface self-assembly technique in an externally applied magnetic field.^[33] A hexane dispersion of NCs (volume: $v = 40$ μ L; concentration: $c = 9$ mg mL⁻¹) containing an excess amount of oleic acid (3 μ L mL⁻¹) was added onto the surface of diethylene glycol (2 mL), inside a polyethylene well of diameter ≈ 2 cm and height ≈ 2 cm. The well was covered with a glass slide to slow down the evaporation of hexane, and immediately placed in an electromagnet with a vertical gradient magnetic field (1200 Oe, gradient 300 Oe cm⁻¹ causing attractive force downward). The whole setup was then left undistributed at room temperature until all the hexane had evaporated (up to ≈ 1 h). The self-assembled magnetic superstructures were transferred onto a Si substrate by lift-off, followed by drying under vacuum to remove residual traces of diethylene glycol. Samples were thereafter thoroughly washed with ethanol by means of a squirt bottle, to remove excess oleic acid surfactant, prior to subsequent characterization in SEM.

Characterization: SEM and STEM micrographs were captured in a Hitachi S-5500 S(T)EM in-lens system, with acceleration voltage and emission current set to be 30 kV and 20 μ A, respectively. TEM micrographs were captured in a JEOL 2100, operating at 200 kV. The field and temperature dependence (after FC and ZFC) of the magnetization was measured using a superconductive quantum interference device (SQUID) magnetometer by Quantum Design. For the dilute dispersion, oleic acid-coated magnetite NCs were dispersed in cyclohexane with concentration <0.1 mg mL⁻¹, and thereafter measured below the fusion point of cyclohexane, with cooling started at 260 °C. The concentration of the dilute dispersion was measured in a Thermo Scientific Element 2 ICP-HR-MS.

Supporting Information

Supporting Information is available from the Wiley Online Library or from the author.

Acknowledgements

The Research Council of Norway is acknowledged for the support to the Norwegian Micro- and Nano-Fabrication Facility, NorFab, project number 245963/F50. We acknowledge support from the Research Council of Norway through the Norwegian Center for Transmission Electron Microscopy, NORTEM (197405/F50), and from the Spanish MINECO through grant number MAT2015-65295-R. This work was partly supported by the Research Council of Norway through its Center

of Excellence funding scheme, project number 262633, “QuSpin”. Syverin Lierhagen is acknowledged for the great assistance with ICP-MS measurements.

Conflict of Interest

The authors declare no conflict of interest.

Keywords

magnetic nanocubes, mechanical stability, self-assembly, spin relaxation, super-size effect

Received: June 16, 2019

Revised: August 3, 2019

Published online:

- [1] T. Wang, X. Wang, D. LaMontagne, Z. Wang, Z. Wang, Y. C. Cao, *J. Am. Chem. Soc.* **2012**, *134*, 18225.
- [2] Z. Zhou, X. Zhu, D. Wu, Q. Chen, D. Huang, C. Sun, J. Xin, K. Ni, J. Gao, *Chem. Mater.* **2015**, *27*, 3505.
- [3] L. Wu, J. J. Willis, I. S. McKay, B. T. Diroll, J. Qin, M. Cargnello, C. J. Tassone, *Nature* **2017**, *548*, 197.
- [4] J. Brunner, I. A. Baburin, S. Sturm, K. Kvashnina, A. Rossberg, T. Pietsch, S. Andreev, E. Sturm (née Rosseeva), H. Cölfen, *Adv. Mater. Interfaces* **2017**, *4*, 1600431.
- [5] S. F. Tan, S. Raj, G. Bisht, H. V. Annadata, C. A. Nijhuis, P. Král, U. Mirsaidov, *Adv. Mater.* **2018**, *30*, 1707077.
- [6] Z. Nie, A. Petukhova, E. Kumacheva, *Nat. Nanotechnol.* **2010**, *5*, 15.
- [7] Y. Liu, J.-J. Yin, Z. Nie, *Nano Res.* **2014**, *7*, 1719.
- [8] T. Ding, K. Song, K. Clays, C.-H. Tung, *Adv. Mater.* **2009**, *21*, 1936.
- [9] L. Shi, L. Zhu, J. Guo, L. Zhang, Y. Shi, Y. Zhang, K. Hou, Y. Zheng, Y. Zhu, J. Lv, S. Liu, Z. Tang, *Angew. Chem., Int. Ed.* **2017**, *56*, 15397.
- [10] L. Zhang, Q. Fan, X. Sha, P. Zhong, J. Zhang, Y. Yin, C. Gao, *Chem. Sci.* **2017**, *8*, 6103.
- [11] K. Bian, H. Schunk, D. Ye, A. Hwang, T. S. Luk, R. Li, Z. Wang, H. Fan, *Nat. Commun.* **2018**, *9*, 2365.
- [12] X. Qiao, B. Su, C. Liu, Q. Song, D. Luo, G. Mo, T. Wang, *Adv. Mater.* **2018**, *30*, 1702275.
- [13] G. Xu, J. Liu, B. Liu, J. Zhang, *CrystEngComm* **2019**, *21*, 411.
- [14] C. Huang, J. Dong, W. Sun, Z. Xue, J. Ma, L. Zheng, C. Liu, X. Li, K. Zhou, X. Qiao, Q. Song, W. Ma, L. Zhang, Z. Lin, T. Wang, *Nat. Commun.* **2019**, *10*, 2779.
- [15] J. J. Urban, D. V. Talapin, E. V. Shevchenko, C. R. Kagan, C. B. Murray, *Nat. Mater.* **2007**, *6*, 115.
- [16] Y. Lalatonne, L. Motte, V. Russier, A. T. Ngo, P. Bonville, M. P. Pileni, *J. Phys. Chem. B* **2004**, *108*, 1848.
- [17] S. Mamica, M. Krawczyk, M. L. Sokolovskyy, J. Romero-Vivas, *Phys. Rev. B* **2012**, *86*, 144402.
- [18] K. E. Mueggenburg, X. M. Lin, R. H. Goldsmith, H. M. Jaeger, *Nat. Mater.* **2007**, *6*, 656.
- [19] Y. Wang, P. Kanjanaboos, S. P. McBride, E. Barry, X. M. Lin, H. M. Jaeger, *Faraday Discuss.* **2015**, *181*, 325.
- [20] N. Goubet, C. Yan, D. Polli, H. Portales, I. Arfaoui, G. Cerullo, M. P. Pileni, *Nano Lett.* **2013**, *13*, 504.
- [21] M. Gauvin, Y. Wan, Arfaoui, M. P. Pileni, *J. Phys. Chem. C* **2014**, *118*, 5005.
- [22] V. Håkonsen, G. Singh, J. He, Z. Zhang, *Mater. Horiz.* **2018**, *5*, 1211.
- [23] Y. Gao, Y. Bao, M. Beerman, A. Yasuhara, D. Shindo, K. M. Krishnan, *Appl. Phys. Lett.* **2004**, *84*, 3361.
- [24] S. Das, P. Ranjan, P. S. Maiti, G. Singh, G. Leitus, R. Klajn, *Adv. Mater.* **2013**, *25*, 422.

- [25] G. Singh, H. Chan, T. Udayabhaskararao, E. Gelman, D. Peddis, A. Baskin, G. Leitus, P. Král, R. Klajn, *Faraday Discuss.* **2015**, *181*, 403.
- [26] C. Jiang, C. W. Leung, P. W. Pong, *Nanoscale Res. Lett.* **2016**, *11*, 189.
- [27] V. Germain, M. P. Pileni, *Adv. Mater.* **2005**, *17*, 1424.
- [28] K. J. Bishop, C. E. Wilmer, S. Soh, B. A. Grzybowski, *Small* **2009**, *5*, 1600.
- [29] C. A. Batista, R. G. Larson, N. A. Kotov, *Science* **2015**, *350*, 1242477.
- [30] S. Mehdizadeh Taheri, M. Michaelis, T. Friedrich, B. Forster, M. Drechsler, F. M. Romer, P. Bosecke, T. Narayanan, B. Weber, I. Rehberg, S. Rosenfeldt, S. Forster, *Proc. Natl. Acad. Sci. USA* **2015**, *112*, 14484.
- [31] M. N. O'Brien, M. R. Jones, C. A. Mirkin, *Proc. Natl. Acad. Sci. USA* **2016**, *113*, 11717.
- [32] X. Bouju, E. Duguet, F. Gauffre, C. R. Henry, M. L. Kahn, P. Melinon, S. Ravaine, *Adv. Mater.* **2018**, *30*, 1706558.
- [33] R. K. Cersonsky, G. van Anders, P. M. Dodd, S. C. Glotzer, *Proc. Natl. Acad. Sci. USA* **2018**, *115*, 1439.
- [34] K. J. Si, Y. Chen, Q. Shi, W. Cheng, *Adv. Sci.* **2018**, *5*, 1700179.
- [35] G. Singh, H. Chan, A. Baskin, E. Gelman, N. Reppin, P. Král, R. Klajn, *Science* **2014**, *345*, 1149.
- [36] J. M. D. Coey, *Magnetism and Magnetic Materials*, Cambridge University Press, Cambridge **2009**.
- [37] A. H. Lu, E. L. Salabas, F. Schuth, *Angew. Chem., Int. Ed.* **2007**, *46*, 1222.
- [38] W. T. Coffey, Y. P. Kalmykov, *J. Appl. Phys.* **2012**, *112*, 121301.
- [39] M. Okuda, T. Schwarze, J. C. Eloi, S. E. Ward Jones, P. J. Heard, A. Sarua, E. Ahmad, V. V. Kruglyak, D. Grundler, W. Schwarzacher, *Nanotechnology* **2017**, *28*, 155301.
- [40] A. Dreyer, A. Feld, A. Kornowski, E. D. Yilmaz, H. Noei, A. Meyer, T. Krekeler, C. Jiao, A. Stierle, V. Abetz, H. Weller, G. A. Schneider, *Nat. Mater.* **2016**, *15*, 522.
- [41] P. Georgopoulos, G. A. Schneider, A. Dreyer, U. A. Handge, V. Filiz, A. Feld, E. D. Yilmaz, T. Krekeler, M. Ritter, H. Weller, V. Abetz, *Sci. Rep.* **2017**, *7*, 7314.
- [42] A. Rinaldi, S. Licoccia, E. Traversa, K. Sieradzki, P. Peralta, A. B. Dávila-Ibáñez, M. A. Correa-Duarte, V. Salgueirino, *J. Phys. Chem. C* **2010**, *114*, 13451.
- [43] A. Rinaldi, M. A. Correa-Duarte, V. Salgueirino-Maceira, S. Licoccia, E. Traversa, A. B. Dávila-Ibáñez, P. Peralta, K. Sieradzki, *Acta Mater.* **2010**, *58*, 6474.
- [44] X. J. Liu, Z. F. Zhou, L. W. Yang, J. W. Li, G. F. Xie, S. Y. Fu, C. Q. Sun, *J. Appl. Phys.* **2011**, *109*, 074319.
- [45] J. N. Plendl, S. S. Mitra, P. J. Gielisse, *Phys. Status Solidi B* **1965**, *12*, 367.
- [46] X. J. Liu, J. W. Li, Z. F. Zhou, L. W. Yang, Z. S. Ma, G. F. Xie, Y. Pan, C. Q. Sun, *Appl. Phys. Lett.* **2009**, *94*, 131902.
- [47] S. Wacke, T. Górecki, C. Górecki, K. Książek, *J. Phys.: Conf. Ser.* **2011**, *289*, 012020.
- [48] J. N. Plendl, P. J. Gielisse, *Phys. Rev.* **1962**, *125*, 828.
- [49] E. Esposito, A. E. Carlsson, D. D. Ling, H. Ehrenreich, C. D. Gelatt, *Philos. Mag. A* **1980**, *41*, 251.
- [50] A. Cornec, I. Scheider, K.-H. Schwalbe, *Eng. Fract. Mech.* **2003**, *70*, 1963.
- [51] G. Gao, X. Liu, R. Shi, K. Zhou, Y. Shi, R. Ma, E. Takayama-Muromachi, G. Qiu, *Cryst. Growth Des.* **2010**, *10*, 2888.
- [52] P. Podsiadlo, G. Krylova, B. Lee, K. Critchley, D. J. Gosztola, D. V. Talapin, P. D. Ashby, E. V. Shevchenko, *J. Am. Chem. Soc.* **2010**, *132*, 8953.
- [53] C. B. Murray, C. R. Kagan, M. G. Bawendi, *Annu. Rev. Mater. Sci.* **2000**, *30*, 545.
- [54] P. Buffat, J. P. Borel, *Phys. Rev. A* **1976**, *13*, 2287.
- [55] E. Ringe, M. R. Langille, K. Sohn, J. Zhang, J. Huang, C. A. Mirkin, R. P. Van Duyne, L. D. Marks, *J. Phys. Chem. Lett.* **2012**, *3*, 1479.
- [56] Y. D. Qu, X. L. Liang, X. Q. Kong, W. J. Zhang, *Phys. Met. Metallogr.* **2017**, *118*, 528.
- [57] P. Hiemenz, R. Rajagopalan, *Principles of Colloid and Surface Chemistry*, CRC Press, Boca Raton, FL **1997**, Ch. 10.
- [58] M. Sánchez-Domínguez, C. Rodríguez-Abreu, in *Nanocolloids: A Meeting Point for Scientists and Technologists* (Ed: C. Rodríguez-Abreu), Elsevier, Amsterdam **2016**, Ch. 1.
- [59] J. B. Smitham, R. Evans, D. H. Napper, *J. Chem. Soc., Faraday Trans. 1* **1975**, *71*, 285.
- [60] R. Evans, J. B. Smitham, D. H. Napper, *Colloid Polym. Sci.* **1977**, *255*, 161.
- [61] A. P. Kaushik, P. Clancy, *J. Chem. Phys.* **2012**, *136*, 114702.
- [62] B. S. Jabes, H. O. Yadav, S. K. Kumar, C. Chakravarty, *J. Chem. Phys.* **2014**, *141*, 154904.
- [63] E. Tam, P. Podsiadlo, E. Shevchenko, D. F. Ogletree, M. P. Delplancke-Ogletree, P. D. Ashby, *Nano Lett.* **2010**, *10*, 2363.
- [64] J. Stöhr, H. C. Siegmann, *Magnetism: From Fundamentals to Nanoscale Dynamics*, Springer-Verlag, Berlin **2006**.
- [65] A. R. Muxworthy, E. McClelland, *Geophys. J. Int.* **2000**, *140*, 101.
- [66] E. Lima, A. L. Brandl, A. D. Arelaro, G. F. Goya, *J. Appl. Phys.* **2006**, *99*, 083908.
- [67] S. Yamamuro, K. Sumiyama, *Chem. Phys. Lett.* **2006**, *418*, 166.
- [68] D. Goll, G. Schütz, H. Kronmüller, *Phys. Rev. B* **2003**, *67*, 094414.
- [69] S. T. Bramwell, M. J. P. Gingras, *Science* **2001**, *294*, 1495.
- [70] M. S. Andersson, R. Mathieu, S. S. Lee, P. S. Normile, G. Singh, P. Nordblad, J. A. Toro, *Nanotechnology* **2015**, *26*, 475703.
- [71] J. A. De Toro, M. Vasilakaki, S. S. Lee, M. S. Andersson, P. S. Normile, N. Yaacoub, P. Murray, E. H. Sánchez, P. Muñiz, D. Peddis, R. Mathieu, K. Liu, J. Geshev, K. N. Trohidou, J. Nogués, *Chem. Mater.* **2017**, *29*, 8258.
- [72] J. A. De Toro, P. S. Normile, S. S. Lee, D. Salazar, J. L. Cheong, P. Muñiz, J. M. Riveiro, M. Hillenkamp, F. Tournus, A. Tamion, P. Nordblad, *J. Phys. Chem. C* **2013**, *117*, 10213.
- [73] H. Mamiya, I. Nakatani, T. Furubayashi, M. Ohnuma, *Trans. Magn. Soc. Jpn.* **2002**, *2*, 36.
- [74] A. J. Rondinone, A. C. S. Samia, Z. J. Zhang, *Appl. Phys. Lett.* **2000**, *76*, 3624.
- [75] A. López-Ortega, E. Lottini, C. de Julián Fernández, C. Sangregorio, *Chem. Mater.* **2015**, *27*, 4048.